

Resources of nonlinear cavity magnonics for quantum information

Mehrdad Elyasi,¹ Yaroslav M. Blanter,² and Gerrit E. W. Bauer^{3,4}

¹*Institute for Materials Research, Tohoku University, 2-1-1 Katahira, 980-8577 Sendai, Japan*

²*Kavli Institute of Nanoscience, Delft University of Technology, Lorentzweg 1, 2628CJ Delft, The Netherlands*

³*Zernike Institute for Advanced Materials, University of Groningen, The Netherlands*

⁴*Institute for Materials Research & AIMR & CSRN, Tohoku University, 980-8577 Sendai, Japan*

We theoretically explore nonlinearities of ferromagnets in microwave cavities in the classical and quantum regimes, and assess the resources for quantum information, i.e. fluctuation squeezing and bipartite entanglement. The (semi-)classical analysis of the anharmonic oscillator (Duffing) model for the Kittel mode when including all other magnon modes, reveals chaotic and limit-cycle phases that do not survive in quantum calculations. However, magnons with nonzero wavenumbers that are driven by the Suhl instability of the Kittel mode, form a genuine limit cycle. We subsequently compute bounds for the distillable entanglement, as well as entanglement of formation for the bipartite configurations of the mixed magnon modes. The distillable entanglement of bipartite states accessible from a covariance matrix vanishes, but can be recovered by injection locking. The predicted magnon entanglement can be experimentally tested with yttrium iron garnet samples under realistic conditions.

I. INTRODUCTION

Cavity optomagnonics is the emergent field devoted to understand the interaction of magnons — the quanta of the elementary spin wave excitations of the magnetic order — with electromagnetic waves confined to cavities [1, 2]. While optomagnonic coupling to (infrared) light is dispersive and, at least to date, rather weak [3–6], magnons (ultra) strongly interact with microwave (MW) photons [1, 2, 7], thereby enabling classical and quantum information processing and storage with coherently controlled magnons [8–11]. Up/down-quantum converters between both communication (optical fibers) and processing (superconducting qubits) units have been envisioned and pursued [3, 4, 12–14].

Strongly coupled MW photons can drive a weakly damped magnonic system easily into the non-linear response regime. Hysteresis [15, 16], Bose-Einstein condensation [17–21], auto-oscillation (and chaos) [22–25], synchronization [26, 27], soliton formation [24, 25, 28–31], and magnon transistors [32] are only few examples of non-linearities in magnetism and magnonics. Microwave cavities facilitate the study of non-linear phenomena by focussing a large number of photons into narrow frequency bands, for example leading to the observation of resonance frequency shifts and bistability in an yttrium iron garnet (YIG) sphere as a function of microwave intensity [33, 34]. These observations were explained with the Duffing model — the minimal model of a non-linear oscillator, with an anharmonic term in the potential energy $\sim x^4$, where x is the canonical position. The Duffing model is the main means to describe non-linearities in the dynamics of nano- and opto-mechanical systems [35–37].

In the linear regime, the dynamics of the fundamental modes of optomechanics and optomagnonics, such as the vibrations of a cantilever and the coherent precession of the magnetic order (Kittel mode) obey basically the same equations. However, while the Duffing model has been found to be quite appropriate for most of non-

linear mechanics, it is not obvious that it should work as well for non-linear magnonics. For example, in contrast to the phonons in elastic media, the magnetic dipolar interaction renders the magnon dispersion in thin films strongly anisotropic and non-monotonic; the Kittel mode at the origin of reciprocal space is not an energetic minimum. The three-field and four-field magnon scattering processes caused by dipolar and exchange interactions, as well as crystalline anisotropies, can lead to instabilities with finite wave lengths that cannot be modelled by a single anharmonic oscillator. Indeed, the unique spin wave dispersion is instrumental to some of the non-linearity induced phenomena such as the generation and observation of non-equilibrium Bose-Einstein (Rayleigh-Jeans) condensation of magnons at nonzero wave vector [17–20, 38], magnonic transistors [32], and instabilities leading to classical auto-oscillation and chaos [15, 22, 23].

On the other hand and in contrast to nanomechanics and Josephson devices, magnonic quantum effects have been elusive with very few possible exceptions [11, 39]. Observation of quantum non-linearities such as squeezing, generation of non-classical states, photon blockade, and entanglement [40–45] have never been reported in magnonics.

Here we argue that transcending the Duffing paradigm is *conditio sine qua non* to explore a considerable potential of optomagnonics for quantum applications. We start by discussing the magnon interactions of strongly driven ferromagnets placed in microwave cavities. We discover not only interesting classical nonlinear dynamics of magnetization, but a variety of previously not investigated quantum effects and discuss how these effects can be used for the field of quantum information. By classical, semi-classical, and quantum calculations we predict different interaction-induced classes of steady states, including a genuinely quantum limit cycle of $\pm \vec{k} \neq 0$ magnon modes. The fluctuation statistics of the steady states reveal squeezing, which can serve as a quantum information resource, as well as bounds for distillable entangle-

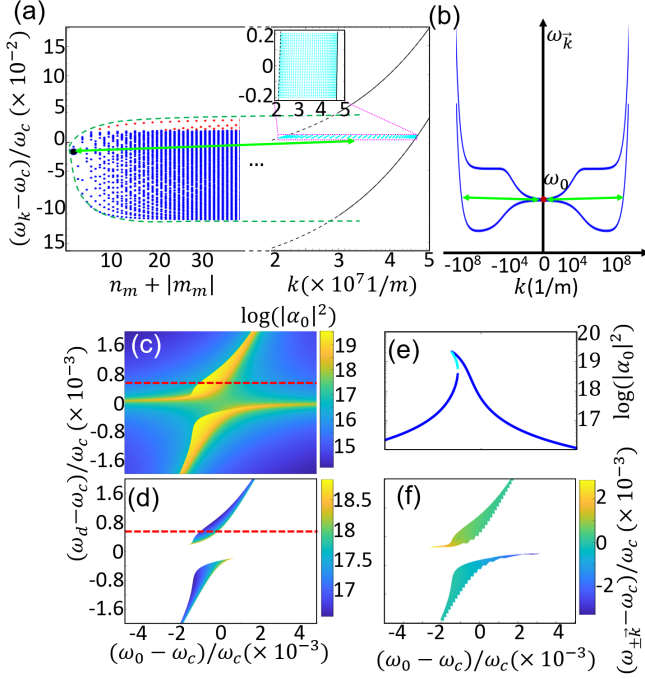


FIG. 1. Kittel mode instability in the Landau-Lifshitz-Gilbert equation. (a) The magnon dispersion for a sphere. The magnetostatic (MS) modes are indicated by black (Kittel mode), blue (bulk modes) and red (surface modes) dots. The MS band matches the continuum band at certain k , at which the green dashed lines touch the black full/dashed lines. The ellipsis \dots indicates the region that separates the continuum from the MS manifold. The cyan-colored dots represent the phase space region tested for instabilities, of which the inset is a zoomed-in version. (b) The envelopes of the magnon dispersion in a thin film on a logarithmic wave number scale. The red dot indicates the Kittel mode. In (a) and (b) the top and bottom envelopes correspond to $\vec{k} \parallel \vec{M}_0 \parallel \hat{z}$ and $\vec{k} \perp \vec{M}_0$, respectively. The green arrows in (a) and (b) schematically depict the four magnon scattering processes (4MS) responsible for the instability of the Kittel mode. (c-e) Steady state solutions for the populated Kittel mode with “self-Kerr” nonlinearity but without inclusion of $\vec{k} \neq 0$ modes. (c) and (d): Magnon number $|\alpha_0|^2$ as a function of Kittel mode and microwave drive frequency, where (c) depicts the solutions when the system is in either stable state or the solution with larger magnon population when the system is bistable, while (d) shows only the solution with smaller magnon numbers in the bistable regime. (e) plots $|\alpha_0|^2$ along the red dashed lines of (c-d). Blue dots are the stable fixed points, and the cyan dots are unstable saddle points. (f) Instability of the Kittel mode solutions in (a) when $\vec{k} \neq 0$ magnons are allowed to contribute. Here the color codes the frequency of the $\pm \vec{k}$ pair that becomes unstable first.

ment and entanglement of formation. Finally, we assess the effect of injection locking of the $\pm \vec{k} \neq 0$ magnons limit cycle on these entanglement measures. As few as four copies of steady states can in principle be transformed into a completely entangled state equivalent to a

spin-singlet, which could be of immediate use in quantum teleportation, simulation, and computation.

In Sec. II, we introduce the details of the model of a magnet inside a cavity and all the nonlinearities involved. Then we classify the outcomes of the nonlinear terms in the anti-crossing region of the magnon Kittel mode and cavity photon frequencies. The outcomes include bistability, Suhl instability, fixed point, limit cycle, and chaotic dynamics of $\pm \vec{k} \neq 0$ magnons. In Sec. III, we include quantum Langevin noise sources, and show that the solutions of $\pm \vec{k} \neq 0$ magnons excited by the Suhl instability of the Kittel mode are always limit cycles. We also develop an equivalent quantum master equation, and solve it in the number space of the corresponding harmonic oscillators. The limit cycle of $\pm \vec{k} \neq 0$ magnons is reproduced in the Wigner function representation of the steady states. In Sec. IV, we address the first quantum information resource, i.e. fluctuation squeezing, which is observable by microwave scattering amplitudes. In Sec. V, we focus on entanglement as an important quantum information resource. We find finite distillable entanglement shared between the Kittel mode and $\pm \vec{k} \neq 0$ modes. However, it is not simply accessible via the covariance matrix of the (quantum) noise, and thereby less interesting from an experimental point of view. In Sec. VIA, we introduce the mechanism of “injection locking” of the $\pm \vec{k} \neq 0$ limit cycle solutions that transforms an arbitrary phase excited state into a fixed point with Gaussian statistics. In Sec. VIB, we show that the distillable entanglement then becomes accessible in the covariance matrix, allowing for a straightforward experimental analysis and utilization of the entanglement. In Sec. VIC, we assess the effect of injection locking on entanglement calculated from the quantum master equation solution, and analyze the consistency with the semiclassical approaches of Sections VIA and VIB. Finally, in Sec. VII, we propose concrete set-ups for experimental realization of the quantum information resources assessed in this work, addressing the key parameters, feasibility, challenges, and constraints on e.g. magnet dimension and environment temperature.

II. MODEL AND CLASSICAL NONLINEAR ANALYSIS

We focus (but do not limit) attention on a high-quality magnetic element such as a sphere (or cube) of yttrium iron garnet in a microwave cavity. The static magnetization \vec{M}_0 is saturated and aligned by an applied static magnetic field $\vec{H}_{ext} \parallel \hat{z}$. The magnet is placed into the antinode of a transverse AC magnetic field of a selected cavity mode with angular frequency ω_c . In the total Hamiltonian

$$H^{(T)} = H^{(c)} + H^{(mc)} + H^{(d)} + H^{(T,m)}, \quad (1)$$

$H^{(c)} = \hbar \omega_c b^\dagger b$, where b (b^\dagger) is the annihilation (creation) operator of a bare photon cavity mode, respec-

tively. $H^{(mc)}$ is the magnon-photon interaction, $H^{(d)} = i\bar{B}(e^{-i\omega_d t}b^\dagger - e^{i\omega_d t}b)$ is the microwave input drive with frequency ω_d and amplitude \bar{B} . $H^{(T,m)} = \sum_{\vec{k}} \hbar\omega_{\vec{k}}c_{\vec{k}}^\dagger c_{\vec{k}} + H_{int}^{(T,m)}$ governs the magnons with annihilation/creation field operators $c_{\vec{k}}/c_{\vec{k}}^\dagger$. The dispersion relation $\omega_{\vec{k}}$ and their interactions $H_{int}^{(T,m)}$ are affected by dipolar field, exchange interaction, and crystalline anisotropy, as summarized in Appendix A [22, 46, 47]. Magnons in the bulk of a magnet are plane waves with wave vector \vec{k} and frequency $\omega_{\vec{k}}$ that start from the Kittel mode at $\vec{k} = 0$ and can be very anisotropic [see Figs. 1(a) and (b)] [48–52]. We treat the finite size effects at wavelengths comparable to the sample size in the Suhl approximation [53], separating the uniform mode from those with finite wavelength that we treat as plane waves. At long wave lengths we may invoke the magnetostatic (MS) approximation [48, 49] to treat the effects of the dipolar interaction. We focus on YIG spheres that are often used in experiments [1, 11], but we can handle magnetic films with minor adjustments.

YIG spheres can be fabricated with diameters down to 250 μm with traditional technology [13, 54]. By integrating YIG into nanoscale photonic chips, further downscaling appears possible [54, 55]. Here, for calculations, we chose a diameter of 0.1 mm, keeping in mind that for larger (smaller) spheres, larger (smaller) drive powers are required to achieve the same results. We adopt a saturation magnetization $M_s = 1.46 \times 10^5 \text{ A/m}$ along the (111) crystalline axis with uniaxial magnetic anisotropy $K_c = -2480 \text{ J/m}^3$ [56], and gyromagnetic ratio $\gamma = 2.11 \times 10^5 \text{ m/(As)}$ [16]. We adopt a cavity mode $\omega_c = 10^{11}/(2\pi) \text{ 1/s}$ and Kittel-cavity mode coupling constant $D_0 = 10 \text{ MHz}$. The magnetization dynamics is damped by a Gilbert constant $\alpha_G = 10^{-4}$ [57] and the dissipation rate of the cavity mode $\zeta_c = 1 \text{ MHz}$ [11]. The magnon interaction in a gas with finite density is described by the Holstein-Primakoff expansion (see Appendix A) in terms of crystalline anisotropies, dipolar and exchange interactions. The leading 3 and 4 particle magnon-magnon scattering processes are conveniently treated in a (Suhl) compartmentalized reciprocal space. The magnon-magnon scattering terms for the Kittel mode are e.g. $c_0^\dagger c_{-\vec{k}} c_{\vec{k}}$ and $c_0^\dagger c_0^\dagger c_{-\vec{k}} c_{\vec{k}}$, where $c_{0(\vec{k})}^\dagger/c_{0(\vec{k})}$ are the creation/annihilation operators of the Kittel and plane-wave ($\vec{k} \neq 0$) magnon modes, respectively. Energy and momentum conservation impose constraints on the ($\vec{k} \neq 0, \omega_{\vec{k}}$) states into which a Kittel mode magnon can be scattered. We assume an external magnetic field \vec{H}_{ext} large enough (much greater than $M_s/3$ for a sphere) such that three magnon, as well as two magnon-one photon scattering processes are non-resonant, which allow us to focus on the effects of four-magnon scatterings (4MS). The degeneracy we exploit here vanishes for very small magnets, so the particle diameter $d \gtrsim 1 \mu\text{m}$.

As discussed in Appendix A, essentially all the dipolar

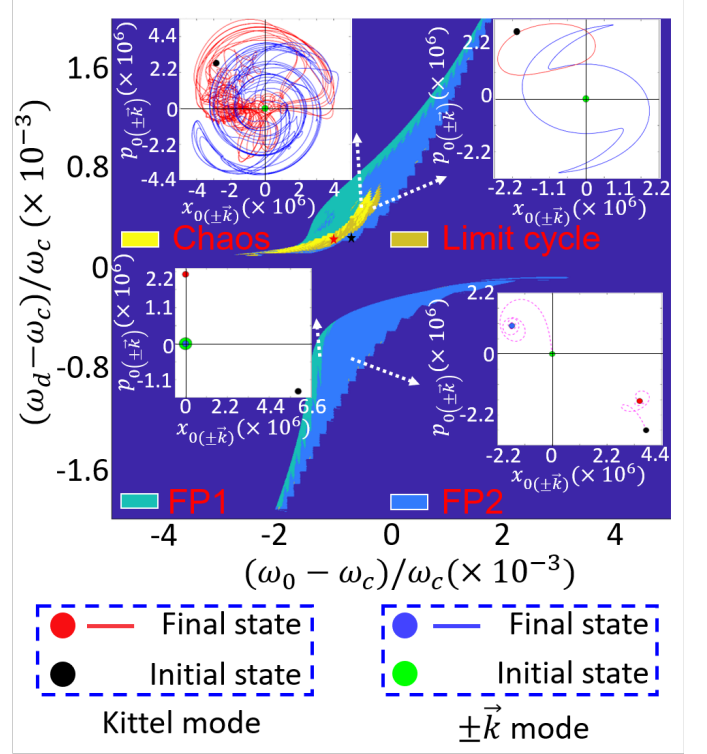


FIG. 2. Steady state classification of the solutions of the Landau-Lifshitz equation without thermal noise. The darkest blue indicates the region where there is no instability of the Kittel mode to $\pm\vec{k} \neq 0$. Each type of steady state is indicated by a color labelled inside the main panel, i.e. chaos, limit cycle, FP1, and FP2. For each of the four types, an example is also shown, and the corresponding point in the main panel map is indicated by white dashed arrows. Point and line colors in inside panels corresponding to initial states and final states are shown in the bottom panel. In FP1 inset, the green point size is adjusted for clarity, and the blue dot coincides with the green dot. The trajectory from initial to final state of FP2 is also shown. The values corresponding to the photonic mode are not shown. The black and red stars in the figure are the (ω_0, ω_d) values used in Fig. 3.

interaction, exchange, and anisotropy contribute to the 4MS terms, see e.g. Eqs. (A10-A14). Here, the exchange interaction maximizes the coefficient of the 4MS term responsible for Suhl instability at large $|\vec{k}|$. The shape anisotropy and crystalline anisotropy contribute a repulsive 4MS interaction. Dipolar interaction and crystalline anisotropy mix the modes, leading to complex 4MS terms [see Eqs. (A18-A20)] such that the label attractive or repulsive cannot be simply made. While the formalism is material independent, we focus here on a parameter set for undoped YIG materials.

The field operators $c_0 = \alpha_0 + \delta c_0$, $c_{\vec{k}} = \alpha_{\vec{k}} + \delta c_{\vec{k}}$ and $b = \beta + \delta b$ fluctuate by $\{\delta c_0, \delta c_{\vec{k}}, \delta b\}$ around the steady state mean field values $\{\alpha_0, \alpha_{\vec{k}}, \beta\}$. The canonical position and momentum (quadrature operators) are $x_{0(\vec{k})} = (c_{0(\vec{k})}^\dagger + c_{0(\vec{k})})/2$ and $p_{0(\vec{k})} = i(c_{0(\vec{k})}^\dagger - c_{0(\vec{k})})/2$ for the

magnon modes and $X = (b^\dagger + b)/2$ and $Y = i(b^\dagger - b)/2$ for the photon mode, respectively, with fluctuations $\delta x_{0(\vec{k})}$, $\delta p_{0(\vec{k})}$, δX , and δY , respectively.

We present results in the (ω_0, ω_d) parameter space for $\bar{B} = 3.3 \times 10^{13} \text{ s}^{-1}$ corresponding to $\sim 1 \text{ mT}$ order of magnitude for dynamic magnetic field exerted on the magnet when $\omega_d \sim \omega_c$. $\bar{B} = \sqrt{\zeta_{c,ex} P_{in} / (\hbar \omega_d)}$, where $\zeta_{c,ex}$ is the photon dissipation by leakage, and the cavity input power $P_{in} \approx 13 \text{ mW}$ (11.1 dBm) for the range of ω_d we consider. This power should be large enough to access all phenomena offered in nonlinear phase space. For smaller powers down to $P_{in} \sim 1 \text{ mW}$, we observe bistability of the Kittel mode and the Suhl instability close to the origing of (ω_0, ω_d) parameter space, but no limit cycles and/or chaotic motion. The power demands scale with the volume of magnet: for a sphere of 1 mm radius, a $P_{in} = 13 \text{ W}$ is necessary to achieve the same results as shown here. Bryant et al. [22] carried out a classical analysis of the full nonlinear dynamics of the Suhl instability of the first kind as a function of input power and dc external magnetic field, at twice the microwave frequency of the Kittel mode. The nonlinear magnetization dynamics of YIG spheres with a typical diameter of 1 mm required powers in the range of 1 – 20 dB (1 – 100 W) [22, 23]. Here we address the Suhl instability of the second kind at excitation frequencies close to the Kittel mode. Experiments that classified the corresponding nonlinear phase space observed limit cycles, and their doublings, eventually leading to chaos [58]. The microwave magnetic fields that cause classical chaos in our analysis is $\sim 2 \text{ mT}$ when $\omega_0 \sim \omega_d$, which agrees with the $\sim 1 - 10 \text{ mT}$ [~ 10 times critical field of Suhl instability [53, 59] of the second kind] in these experiments and theories [23, 58].

The equations of motion (EOM) for the three distinct fields (and similarly for the hermitian conjugates), viz. the cavity mode field, Kittel mode field, and selected $\vec{k} \neq 0$ modes fields, is obtained from $H^{(T)}$ [see Eq. (1) and Appendix A], with dissipation and noise added:

$$\begin{aligned} \dot{c}_0 = & -i \left(\Delta_0 + 2 \sum_{\vec{k} \neq 0} \text{Re} [\mathcal{D}_{0,\vec{k}}^{4MS,1}] n_{\vec{k}} \right) c_0 - \frac{\zeta_{m,0}}{2} c_0 \\ & - 2i c_0^\dagger \sum_{\vec{k} \neq 0} \mathcal{D}_{0,\vec{k}}^{4MS,2} c_{-\vec{k}} c_{\vec{k}} - \\ & 2i \text{Re} [\mathcal{D}_{0,0}^{4MS,1} + \mathcal{D}_{0,0}^{4MS,2}] [c_0 + 2c_0^\dagger c_0] + i D_0 b + \\ & \sqrt{\zeta_{mm,0}} F_{mm,0}(t) + \sqrt{\zeta_{mp,0}} F_{mp,0}(t), \end{aligned} \quad (2)$$

$$\begin{aligned} \dot{c}_{\vec{k} \neq 0} = & -i \left(\Delta_{\vec{k}} + 2 \sum_{\vec{k}' \neq \vec{k}} \text{Re} [\mathcal{D}_{\vec{k},\vec{k}'}^{4MS,1}] n_{\vec{k}'} \right) c_{\vec{k}} - \frac{\zeta_{m,\vec{k}}}{2} c_{\vec{k}} \\ & - i (\mathcal{D}_{0,\vec{k}}^{4MS,2})^* c_0 c_0^\dagger - 2i \text{Re} [\mathcal{D}_{\vec{k},\vec{k}}^{4MS,1}] [c_{\vec{k}} + 2c_{\vec{k}}^\dagger c_{\vec{k}}] \\ & - i c_{-\vec{k}}^\dagger \sum_{\vec{k}' \neq 0} \mathcal{D}_{\vec{k},\vec{k}'}^{4MS,2} c_{-\vec{k}'} c_{\vec{k}'} \\ & + \sqrt{\zeta_{mm,\vec{k}}} F_{mm,\vec{k}}(t) + \sqrt{\zeta_{mp,\vec{k}}} F_{mp,\vec{k}}(t), \end{aligned} \quad (3)$$

$$\begin{aligned} \dot{b} = & -i \Delta b - \frac{\zeta_c}{2} b + B + i D_0 c_0 + \\ & \sqrt{\zeta_{c,0}} F_{c,0}(t) + \sqrt{\zeta_{c,ex}} F_{c,ex}(t), \end{aligned} \quad (4)$$

where $\mathcal{D}_{\vec{k}',\vec{k}''}^{4MS,1}$ and $\mathcal{D}_{\vec{k}',\vec{k}''}^{4MS,2}$ are the strengths of the 4MS scatterings of the form $c_{\vec{k}'}^\dagger c_{\vec{k}''}^\dagger c_{\vec{k}'} c_{\vec{k}''}$ and $c_{\vec{k}'}^\dagger c_{-\vec{k}'}^\dagger c_{\vec{k}''} c_{-\vec{k}''}$, respectively (see Appendix A). We defined detunings $\Delta_0 = \omega_0 - \omega_d$, $\Delta_{\vec{k}} = \omega_{\vec{k}} - \omega_d$, and $\Delta = \omega_c - \omega_d$. The damping parameters are $\zeta_{m,0} = \zeta_{mm,0} + \zeta_{mp,0}$, $\zeta_{m,\vec{k}} = \zeta_{mm,\vec{k}} + \zeta_{mp,\vec{k}}$, and $\zeta_c = \zeta_{c,ex} + \zeta_{c,0}$. $\zeta_{mm,0}$ ($\zeta_{mp,0}$) is the dissipation rate of the Kittel mode field by interaction with the magnon (phonon) bath, and $\zeta_{mm,\vec{k}}$ ($\zeta_{mp,\vec{k}}$) the same for the \vec{k} mode. $\zeta_{c,ex}$ ($\zeta_{c,0}$) is the photon dissipation by leakage (interaction). The damping parameters ζ_X are connected to the stochastic (Markovian) Langevin fields F_X by the fluctuation dissipation theorem. Details are given in Appendix B.

The nonlinearity of the Kittel mode alone is the so-called self-Kerr term $(c_0^\dagger c_0)^2$, which corresponds to the non-parabolicity in the Duffing model. It leads to a bistability in the solutions of the classical mean fields when \bar{B} exceeds a certain threshold, which happens here in (ω_0, ω_d) parameter space close to the magnon-polariton ($\omega_0 = \omega_d$) [33, 34, 60]. We address this reduced problem by the EOM of Eqs. (2-4), by dropping all terms involving the $\vec{k} \neq 0$ magnons and replace the stochastic fields by their mean values, which leads to a sixth order equation in $|\alpha_0|^2$ (α_0 is the Kittel mode mean field). Our choice for \bar{B} is above the threshold, and two stable and one unstable (saddle point) solutions of $|\alpha_0|^2$ manifest the classical bistability. Figures 1(c)-(e) show a typical map of the computed “self-Kerr” solution, i.e. the Kittel magnon number $|\alpha_0|^2$ without mixing with other modes. Figure 1(c) summarizes the stable solutions and the large amplitude or number state in the parameter regime in which the system is bistable, i.e. close to the magnon-polariton (anti)crossing, while Figure 1(d) is the other stable solution with smaller magnon numbers. Note that we evaluate the complete nonlinear phase space at each (ω_0, ω_d) independently, thereby disregarding (classical) hysteretic effects that arise when cycling e.g. the applied magnetic field (i.e. ω_0). Figure 1(e) is a plot of the frequencies of the stable and unstable (saddle points) solutions for the ω_d indicated by red-dashed lines in Figs. 1(c) and 1(d).

Subsequently, we assess the Suhl instability of the solutions in Fig. 1(c) caused by 4MS with $\vec{k} \neq 0$ magnons (for the parameters used here, the lower magnon number solutions in Fig. 1(d) remain stable). We scan the \vec{k} values for which the 4MS is expected to be largest (see Fig. 1(a)) and search for the $\pm \vec{k} \neq 0$ pair of modes with largest positive real eigenvalue of the linearized matrix \mathcal{O} (defined in Appendix B) that here corresponds to the EOM linearized around the Kittel mode mean field. Results are summarized in Fig. 1(f) in the form of the frequencies of the most unstable magnon pairs $\omega_{\pm \vec{k}}$.

In order to classify the steady states, we first solve the EOM, i.e. Eqs. (2-4) without Langevin stochastic fields, in which the field operators become classical amplitudes, similar to conventional micromagnetics. The solutions of the EOM with initial condition chosen to be an excited pure Kittel mode from Fig. 1(c) are shown in Figure 2. We observe (i) chaotic behavior with finite positive Lyapunov exponents [61, 62], (ii) limit cycle (LC), and (iii) fixed point (FP1 and FP2) solutions. The final state in region FP1 is a pure Kittel mode, which implies that the self-Kerr solution from the higher magnon number branch relaxes back to the stable lower magnon number one in Fig. 1(d): The $\vec{k} \neq 0$ modes help the Kittel mode to explore a larger phase space, thereby escaping a fixed point with a shallow energy well. In region FP2 the system settles into a hybrid state with significant contributions from magnons with finite momentum.

III. QUANTUM LANGEVIN AND MASTER EQUATION

Next, we solve the EOMs with random initial conditions close to those of Fig. (2) and add Langevin quantum stochastic fields at an ambient temperature $T_{\text{env}} = 1$ K (see Eqs. (2-4) and Appendix B2 for description of baths and their correlation functions, moderate temperature variations cause expected and mild changes). Since the (Markovian) bath approximation breaks down as $T_{\text{env}} \rightarrow 0$, we cover the ultra-low temperature regime by solving the quantum master equations for $T = 0$ K (see also Appendix C). We conclude below that the features such as entanglement measures (see Sec. VI) are mathematically (and physically) tolerant with respect to moderate changes in temperature. We repeat the computations 1600 times for the (ω_0, ω_d) points of Figure 2 indicated by black and red stars, i.e. a fixed point of type 2 (FP2), with results in Figure 3(a), and of a limit cycle (LC) with results in Figure 3(b), respectively. We plot the probability distributions of $\{\langle x_0(p_0) \rangle, \langle X(Y) \rangle, \langle x_{\pm\vec{k}}^2 + p_{\pm\vec{k}}^2 \rangle\}$, where $x_0 = \text{Re}[\alpha_0]$, $p_0 = \text{Im}[\alpha_0]$ for the Kittel mode, X, Y are the analogues for the photon (for completeness), and $|\alpha_{\pm\vec{k}}|^2 = x_{\pm\vec{k}}^2 + p_{\pm\vec{k}}^2$ is the number of $\pm\vec{k}$ magnons. The phase of $\alpha_{\pm\vec{k}}$ for FP2 in Figure 3(a) becomes undetermined. Even though the steady state solution of $\vec{k} \neq 0$ magnons is a fixed point, the noise transforms it to a limit cycle. The Kittel and photon modes, on the other hand, undergo only a coherent precession with small and elliptical fluctuations while their phases remain deterministic. Figure 3(b) shows the fate of a LC after the noise is switched on. The averages of the $\vec{k} \neq 0$ magnons are distributed over a doughnut in phase space [a typical trajectory is plotted as pink dashed line in Figure 3(b)]. The dynamics of the Kittel and photon mode are still the same deterministic LC closed loops of the noiseless solutions. The inset of Fig. 3(a) shows the probability dis-

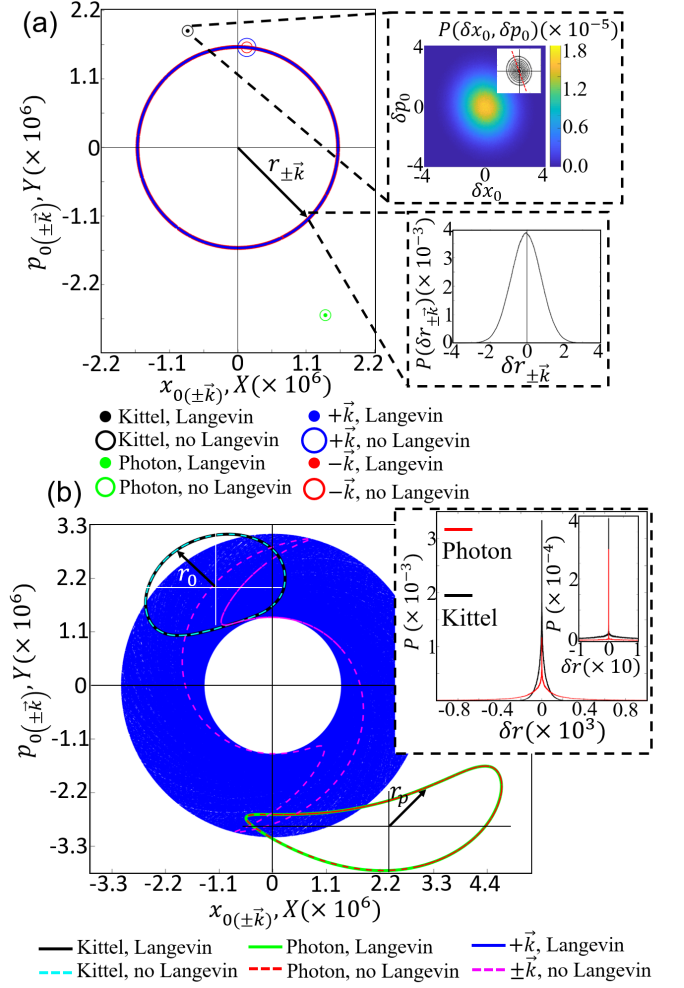


FIG. 3. Steady states of the system with inclusion of Langevin fields. (a) and (b) correspond to FP2 and LC, at (ω_0, ω_d) indicated by black and red stars in Fig. 2, respectively. (a) Main panel is the final fixed points with and without inclusion of Langevin fields for the Kittel, $\pm\vec{k}$, and photon modes. The final states for all the 1600 runs with Langevin fields, plotted. Insets show probability distributions of the fluctuations. In the panel for $P(\delta x_0, \delta p_0)$, the inset is contour plot, and the red dashed line indicates the long axis of the fluctuation ellipse. (b) Main panel shows the trajectory of all the modes in the last $2 \mu\text{s}$ of all the 1600 runs with Langevin fields. The trajectories of steady states without Langevin fields also shown. The inset shows the probability distribution of photon and Kittel modes. In (a) and (b), the probability distribution is evaluated over the fluctuations in the width of the limit cycles, i.e. $\delta r_{\pm\vec{k}}$, δr_0 , and δr_p , averaged over the cycle loop. In each panel, $r_{\pm\vec{k}}$, r_0 , and r_p indicate $\pm\vec{k}$, Kittel, and photon modes limit cycles with respect to their corresponding centers. Centers of each limit cycle is crossing of global/local axes shown.

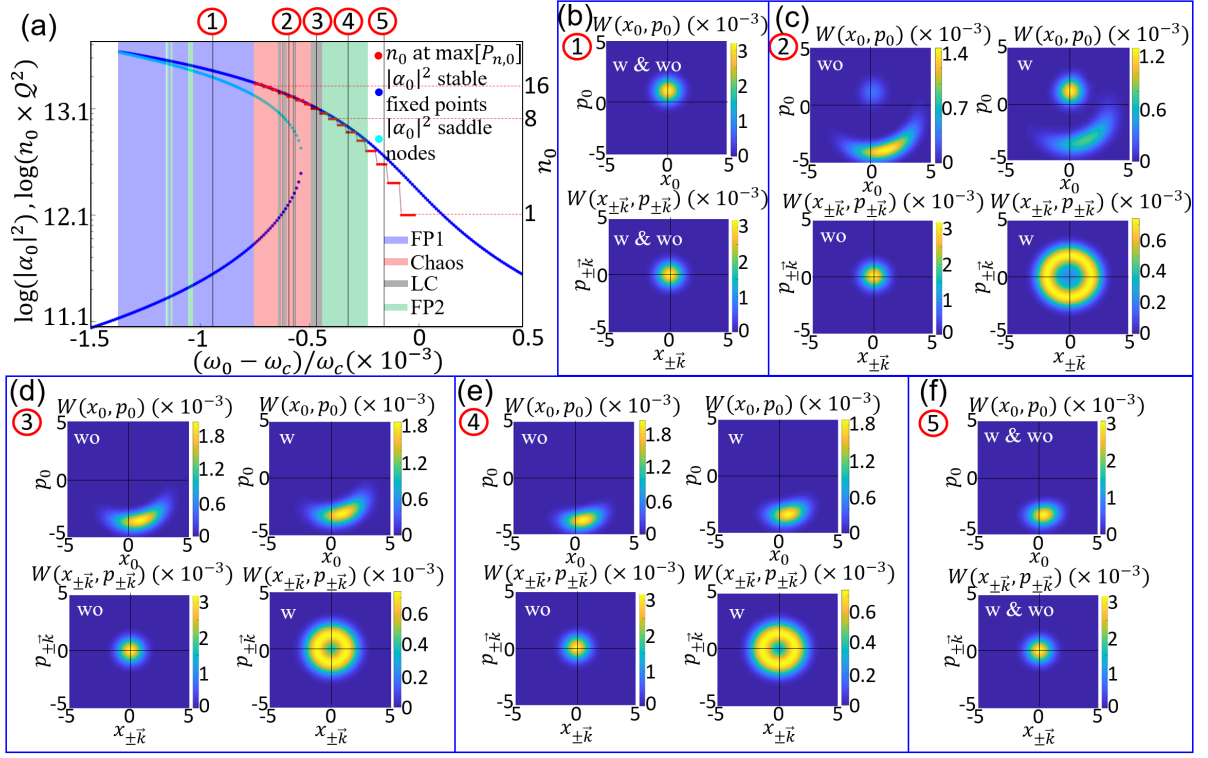


FIG. 4. Steady states derived from the quantum master equation. (a) Duffing model: n_0 , the maximum of the number distribution $P_{n,0}$ of the Kitten mode compared with the classical magnon number ($|\alpha_0|^2$) from Fig. 1(e) for the photon frequency ω_d , indicated by the red-dashed line in Figs. 1(c) and (d). The right vertical ordinate indicates n_0 as solved in the scaled system, whereas the left axis shows the corresponding values in the physical basis. The different classes of steady states when $\vec{k} \neq 0$ modes are included are coded by the background shading colors (see Fig. 2). Five particular magnetic fields (ω_0) are singled out by the numbered vertical thin black lines. (b)-(f) Wigner function [Eq. (6)] for the Kitten and $\pm\vec{k}$ modes [‘w’(‘wo’) means with(out) inclusion of $\pm\vec{k}$ modes].

tribution P of the fluctuations around the mean field of the Kitten and $\pm\vec{k}$ modes. Since the mean-field Kitten (or photon) mode is a fixed point, the fluctuation probability distribution in $(\delta x_0, \delta p_0)$ space is expected to be Gaussian. The radial fluctuations $P(\delta r_{\pm\vec{k}})$ of the $\pm\vec{k}$ limit cycle solutions are also Gaussian distributed. On the other hand, the fluctuations around the Kitten (photon) mode limit cycles in the inset of Fig. 3(b) are clearly not Gaussian. The width of the distribution is larger by a factor of $\sim 10^3$ than the Gaussians of Fig. 3(a) that correspond to the environment temperature $T_{env} = 1$ K. The probability distribution is the deviation from the trajectory, and in principle independent of its form. The relatively large width of the distribution appears nevertheless to be correlated with the complexity of the deterministic LC, and the increased noise smear out the structure in phase space. We see below that these LC’s do not exist in the quantum master equation calculations, indicating that the quantum fluctuations have more serious effects than the thermal ones at 1 K.

Finally, we turn to quantum effects by solving the mas-

ter equation

$$\dot{\hat{\rho}} = -i[H'(T), \hat{\rho}] + \sum_{\vec{k}' \in \{0, \vec{k}, -\vec{k}\}} L_{\vec{k}'}^{(T)}(\hat{\rho}, T_{env}), \quad (5)$$

where in $H'(T)$ the photon mode has been adiabatically removed from $H^{(T)}$, with renormalized Kitten mode detuning $\Delta'_0 = [\Delta_0 - (D_0^2 \Delta)/(\Delta^2 + \zeta_c^2/4)]$ and Kitten mode drive $i(\bar{B}'c_0^\dagger - h.c.)$ with effective field $\bar{B}' = (-i\Delta\bar{B}D_0)/(\Delta^2 + \zeta_c^2/4)$, where Δ is cavity detuning with respect to drive and ζ_c the cavity damping. $L_{\vec{k}'}^{(T)}(\hat{\rho}, T_{env})$ is the total Lindblad operator for each of the magnon modes. This master equation is based on the assumption of Markovian baths. Equation (5) can be rewritten in terms of a super-operator \mathcal{L} as $\dot{\hat{\rho}} = \mathcal{L}\hat{\rho}$ and the steady state density matrix ρ_{ss} is the solution of $\mathcal{L}\rho_{ss} = 0$. We can compute the eigenvector of the sparse matrix \mathcal{L} corresponding to the lowest eigenvalue (see Appendix C) for a matrix dimension of up to $10^6 \times 10^6$. Even at $T_{env} = 0$ this forces us to scale the system down to a numerically tractable Hilbert space, dividing \bar{B} by a factor Q while multiplying the fourth order interactions by Q^2 . This scaling preserves the bistability map as well as instabil-

ity with respect to $\pm\vec{k}$ magnon generation in the (ω_0, ω_d) parameter space. The cost-benefit ratio of the scaling is optimized by $\mathcal{Q} = 1.1 \times 10^6$. Calculations for finite temperatures are possible but expensive, and for this scaling amplitude, we expect only weak effects for $T_{\text{env}} \lesssim 0.1 \text{ K}$.

We first focus on the quantum mechanical Duffing oscillator, without mixing in $\pm\vec{k}$ magnons. Figure 4(a) summarizes the calculated $|\alpha_0|^2$, as well as the $n_0 = c_0^\dagger c_0$ which maximizes the number distribution for a fixed photon frequency, and ω_d corresponding to Fig. 1(e). The left axis shows $|\alpha_0|^2$ and the rescaled $n_0 \mathcal{Q}^2$ to facilitate comparison with the classical results, while the right axis is n_0 in the downscaled system. The discrete steps in n_0 are an artifact introduced by the small size of the rescaled system. The colored background encodes the type of the corresponding classical steady state. The numbered vertical lines indicate the selected drive frequencies for which we compute the steady state density matrix ρ_{ss} including the $\vec{k} \neq 0$ magnon modes. The reduced density matrix for each mode $\rho_{\vec{q}}$ is obtained by tracing out all other modes, i.e. $\rho_{\vec{q}} = \text{Tr}_{\vec{q}' \neq \vec{q}}[\rho_{ss}]$, where $\vec{q}', \vec{q} \in \{0 \text{ (Kittel magnon)}, \pm\vec{k}\}$. We calculate the Wigner function, a (quasi-)probability distribution in position-momentum phase space [63, 64],

$$W(x_{\vec{q}}, p_{\vec{q}}) = \int \left\langle x_{\vec{q}} - \frac{y}{2} \left| \hat{\rho}_{\vec{q}} \left| x_{\vec{q}} + \frac{y}{2} \right\rangle e^{ip_{\vec{q}}y} dy, \quad (6)$$

where $|x_{\vec{q}} \pm \frac{y}{2}\rangle$ are position eigenstates. Results are summarized in Figures 4(b)-(f), representing the distinct classes (FP1, chaos, LC, FP2, and stable to 4MS, respectively) found in the (semi-)classical calculations. While chaos and limit cycles of the Kittel and photon modes do not survive in the quantum regime, the limit cycle in the $\pm\vec{k} \neq 0$ modes become conspicuous as rings in Figs. 4(c)-(e). The maxima of the Wigner functions should be interpreted as attractors (fixed point or limit cycle) that are broadened by zero-point (and in case of $T_{\text{env}} \neq 0$ thermal) fluctuations. A fixed point with (squeezed) thermal fluctuations such as the Kittel mode solution in Fig. 3(a) becomes a Gaussian in the Wigner function centered on the same point of phase space, e.g.

$$W(x_0, p_0) = \frac{1}{\pi(n_{th} + \frac{1}{2})} \exp\left(-\frac{|x_0 + ip_0 - \alpha_0|^2}{n_{th} + \frac{1}{2}}\right) \quad (7)$$

for an isotropic coherent state [63, 64]. In the present quantum calculations, we address the zero-point fluctuation with $n_{th} \rightarrow 0$. The probability distribution of the position and momentum $P(\delta x_0, \delta y_0)$ (see e.g. Fig. 3(a) insets) is related to the Wigner function as $P(\delta x'_{0,\theta}) = \int_{-\infty}^{+\infty} W(\delta x'_0, \delta p'_0) d\delta p'_0$, where $(\delta x'_{0,\theta}, \delta p'_{0,\theta})$ corresponds to $(\delta x_0, \delta p_0)$ rotated by θ . For a Gaussian, $P(\delta x_0, \delta p_0) = W(\delta x_0, \delta p_0)$. In general, the Wigner function can be reconstructed from a measured P by e.g. a maximum likelihood or Radon transform [66]. The limit cycle of $\pm\vec{k}$ modes in Fig. 3(a) is a circle with

the same radius and width as the corresponding Wigner function at the same T_{env} . $W(x_0, p_0)$ in Fig. 4(c) shows two local maxima pertaining to two classically bistable points [60, 65]; the self-Kerr bistability is a classical phenomenon, while quantum fluctuations lead to finite distributions around the two fixed points in phase space.

IV. SQUEEZING OF THE NOISE

Since the quantum analysis rules out limit cycles in the steady state of the Kittel (photon) mode, we may analyze their nature by focussing on the phase space in the proximity of the fixed points FP1 and FP2, which is accessible in terms of the steady state covariance matrix Λ_∞ (see Appendix B for details), and experimentally in the cavity output field, e.g. by homodyne detection [64, 66]. In Figs. 5(a) and 5(b), we map the angle of the minor axis θ_{sq} and ellipticity ξ_{sq} of the calculated variances. Figure 5(c) shows some examples of the *photonic* Wigner functions obtained from the covariance matrices calculated by the quantum Langevin equations (non-scaled system with $T_{\text{env}} = 1 \text{ K}$) [64, 67] as

$$W(\delta X, \delta Y) = \int_{-\infty}^{+\infty} d^3\delta x_{0(\pm\vec{k})} d^3\delta p_{0(\pm\vec{k})} \frac{1}{(2\pi)\sqrt{\det(\Lambda_\infty)}} \times \exp\left\{-\frac{1}{2}\mathbf{v}\Lambda_\infty\mathbf{v}^T\right\}, \quad (8)$$

where $\mathbf{v} = [\delta x_0, \delta p_0, \delta x_{\vec{k}}, \delta p_{\vec{k}}, \delta x_{-\vec{k}}, \delta p_{-\vec{k}}, \delta X, \delta Y]$. $d^3\delta x_{0(\pm\vec{k})} = d\delta x_0 d\delta x_{\vec{k}} d\delta x_{-\vec{k}}$, and $d^3\delta p_{0(\pm\vec{k})} = d\delta p_0 d\delta p_{\vec{k}} d\delta p_{-\vec{k}}$. Here, the black contours are the computed variance ellipses, while the red circles indicate the zero-point fluctuations of the non-interacting photon. This analysis only holds for fixed points, otherwise the full Wigner function as in Figs. 4(b)-(f) should be computed. For a classical state, the uncertainty in a given direction in the position-momentum (quadrature) phase space can not be less than 1, which implies that the black and red contours may not intersect. The two panels of Fig. 5(c) that are marked by purple stars are therefore proof-of-principle that quantum squeezed states can be generated. This magnon-induced squeezing of light is the first quantum information resource reported here. It is an essential ingredient for accurate measurements of e.g. sub-shot-noise phases in a Mach-Zehnder setup [64]. At certain points in the (ω_0, ω_d) plane, the amount of squeezing can be enhanced by increasing the power (i.e. $|\alpha_{0,\pm\vec{k}}|$, see Appendix B 1) as well as reducing T_{env} .

V. ENTANGLEMENT

A second resource for quantum information is entanglement. The 4MS term of the form $c_0^\dagger c_0 c_{\vec{k}}^\dagger c_{\vec{k}} + c_0^\dagger c_0 c_{-\vec{k}}^\dagger c_{-\vec{k}}$ leads to a dominant mean-field potential $\alpha_0 \alpha_{\vec{k}} \delta c_0^\dagger \delta c_{\vec{k}}^\dagger +$

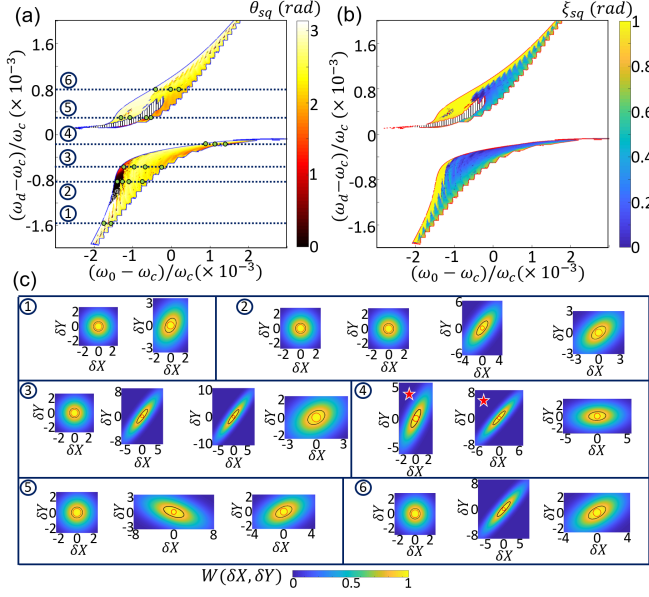


FIG. 5. Fluctuation ellipticity from steady state covariance matrix when $\vec{k} \neq 0$ modes are included. (a) Fluctuation variance ellipse angle θ_{sq} . (b) Fluctuation variance ellipticity ξ_{sq} . In (a) and (b), the hatched area is where the classical steady state is a limit cycle or chaos (see Fig. 2). (c) The constructed Wigner function of the fluctuation for the cavity mode, $W(\delta X, \delta Y)$, from covariance matrix. Each numbered section in (c) corresponds to ω_d indicated by a dashed line with the same number, and ω_0 of each panel is indicated by a hollow circle on the corresponding dashed line (the left most panel of each section: case with smallest ω_0). The colormap is the same for all the panels, and normalized to the max value of each panel.

$\alpha_0 \alpha_{-\vec{k}} \delta c_0^\dagger \delta c_{-\vec{k}}^\dagger + \text{h.c.}$, i.e. a “two-mode squeezing” Hamiltonian for the Kittel and either mode of the $\pm \vec{k}$ pair, which corresponds to the maximal bipartite entanglement of two continuous variables [67, 68]. When the instability mixes Kittel with $\pm \vec{k}$ modes, i.e. $\alpha_{\pm \vec{k}} \neq 0$, the modes should be entangled. Correspondingly, a 4MS term of the form $c_0 c_0 c_{\vec{k}}^\dagger c_{-\vec{k}}^\dagger + c_{\vec{k}}^\dagger c_{\vec{k}} c_{-\vec{k}}^\dagger c_{-\vec{k}} + \text{h.c.}$ should entangle the $\pm \vec{k}$ modes. In order to assess entanglement, we consider the two distinct bipartite configurations as sketched in Fig. 6, (i) the Kittel magnon-photon polariton as one part and the $\pm \vec{k}$ pair as the other, and (ii) one of the modes of the $\pm \vec{k}$ pair, say \vec{k} , considered as one part and $-\vec{k}$ plus the Kittel magnon-photon polariton as the other. It should be reminded that the Kittel mode and the cavity photon form a hybridized mode, polariton, due to the strong coupling through the beam splitter interaction $i c_0 b^\dagger + \text{h.c.}$, and can be considered as one part. For applications such as quantum teleportation [69, 100], the entanglement of distillation E_D , i.e. the rate of entanglement (number of perfect Einstein-Podolsky-Rosen states [68] such as spin singlets) is an important parameter. It can be extracted from a bipartite state by local opera-

tions and classical communication (the so-called LOCC protocols) [67, 70–72]. Here we employ the concept of negative partial transposition (NPT) [73, 74]: the existence of negative eigenvalues of a bipartite state density matrix $\rho_1 \otimes \rho_2$ after partial transposition $(\rho_1)^T \otimes \rho_2$ is a sufficient condition for an entangled state, for bipartite Gaussian states even a necessary one [67]. The degree of negativity in the partial transposed density matrix can be quantified by the logarithmic negativity E_{LN} which determines the upper bound of E_D [67, 75]. In other words, depending on the LOCC protocols used for purification of entanglement of a general mixed state of a bipartite configuration, a maximum number of $E_{LN} \times N$ entanglement bits (number of spin-singlets) can be distilled, where N is the number of copies of the bipartite state. We are therefore interested in the logarithmic negativity E_{LN} [67, 70, 73–75] of both our semi-classical and quantum density matrices. The former is calculated from the covariance matrix and the latter directly from the density matrix in the number space of involved modes (see Appendix C). Another measure is the entanglement of formation E_F , i.e. the number of fully entangled bipartite particles (such as a spin-singlet) required to form the state, or in other words the minimum of the von Neumann entropy of the bipartite state among different (infinite) realizations of a mixed state. We compute E_F for completeness, but note that in contrast to E_D , its value is not of practical importance. The details of the calculations for both approaches to the density matrix are deferred to Appendix D, which also provides a short review of the entanglement measures used here.

Unfortunately, we find that the covariance matrix extracted from the Langevin formalism leads to $E_{LN,0\{\pm \vec{k}\}}^L = 0$ (superscript L stands for Langevin) all over the (ω_0, ω_d) map: The trace over one mode of an imperfect two-mode squeezed state leads to a (broadened) squeezed coherent state with an almost deterministic phase. Moreover, the relative position and total momentum of a two-mode squeezed state is also (almost) deterministic. For example, when the bipartite state of the Kittel mode and, say, $+\vec{k}$ mode of the $\pm \vec{k}$ pair is close to a two-mode squeezed state, $x_0 - x_{+\vec{k}}$ and $p_0 + p_{+\vec{k}}$ should be deterministic. However, since the attractors of the $\pm \vec{k}$ modes are limit cycles [see Fig. 3(a) and Figs. 4(c)-(e)], while that of the Kittel mode is a fixed point, $x_0 - x_{+\vec{k}}$ and $p_0 + p_{+\vec{k}}$ are undetermined, no distillable continuous variable entanglement should be expected. The analysis based on the covariance matrix is only accurate for Gaussian states or continuous variable entanglement [67], so $E_{LN}^L = 0$ does not contradict the finite distillable bipartite entanglement found in the quantum solutions of the scaled system, which indicate that the states are non-Gaussian. For example, at (ω_0, ω_d) indicated by the black star in Fig. 2 (all the results in Fig. 7 and Fig. 8 correspond to this point), $E_{LN,0\{\pm \vec{k}\}}^q \sim 0.3$ and $E_{LN,\pm \vec{k}\{0,\mp \vec{k}\}}^q \sim 0.4$ (superscript q stands for quan-

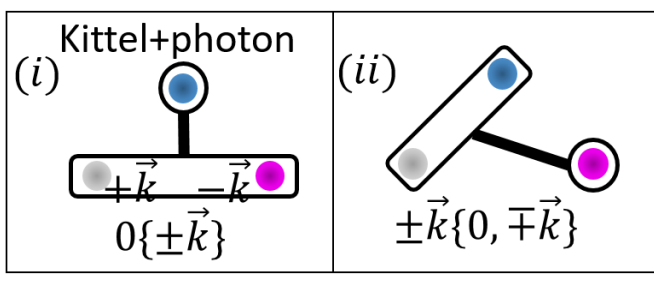


FIG. 6. The two distinct bipartite configurations of the essentially tripartite system, i.e. (i) $0\{\pm\vec{k}\}$ and (ii) $\pm\vec{k}\{0, \mp\vec{k}\}$.

tum), whereas the continuous variable entanglements $E_{LN,0\{\pm\vec{k}\}(LN,\pm\vec{k}\{0,\mp\vec{k}\})}^L = 0$. In other words, entangled states of continuous variables do not comprise all of the entanglement conceivable from bosonic modes. For two modes, a state such as $|0, N\rangle + |N, 0\rangle$ (0 is the vacuum Fock state in one mode and N is the N 'th Fock state in the other mode) is a maximally entangled state [76] but not a two-mode squeezed state.

VI. DISTILLABLE GAUSSIAN ENTANGLEMENT

The finite distillable entanglement by non-Gaussian states predicted for the driven magnet can be assessed experimentally only by a full reconstruction of the density matrix, which is technically very challenging. Only very recently techniques for quantum state tomography of Gaussian states in microwave frequencies have been developed (see below). On the other hand, Gaussian states are fully characterized by the second moment or the auto and cross-correlations which are more readily measured and sufficient to assess the continuous variable entanglement. However, this requires getting rid of the limit cycles. This can be achieved by fixing the phases of the $\pm\vec{k}$ modes via “injection locking” [24, 40, 77, 78] by an AC coherent drive with fixed phase, a standard technique used e.g. to improve current-induced spin oscillations [78].

A. Injection locking of $\pm\vec{k} \neq 0$ magnons

Here we study a spatially modulated injection locking with Hamiltonian $H_l = i(B_l e^{-i\omega_L t} c_{\pm\vec{k}}^\dagger - B_l^* e^{i\omega_L t} c_{\pm\vec{k}})$ with drive frequency $\omega_L = \omega_{\pm\vec{k}}$ and amplitude $B_l = |B_l| \exp(i\phi_l)$ and phase ϕ_l , which couples to both modes of the $\pm\vec{k}$ pair. Large enough B_l transforms limit cycles into fixed points, in both the semi-classical [see Fig. 7(a)] and quantum calculations [see Fig. 7(b)]. Figure 7(c) illustrates the effect of locking as a function of $|B_l|$ and a fixed phase $\phi_l = 0$. With increasing $|B_l|$, the mean number of $\pm\vec{k}$ magnons increases, whereas the numbers of

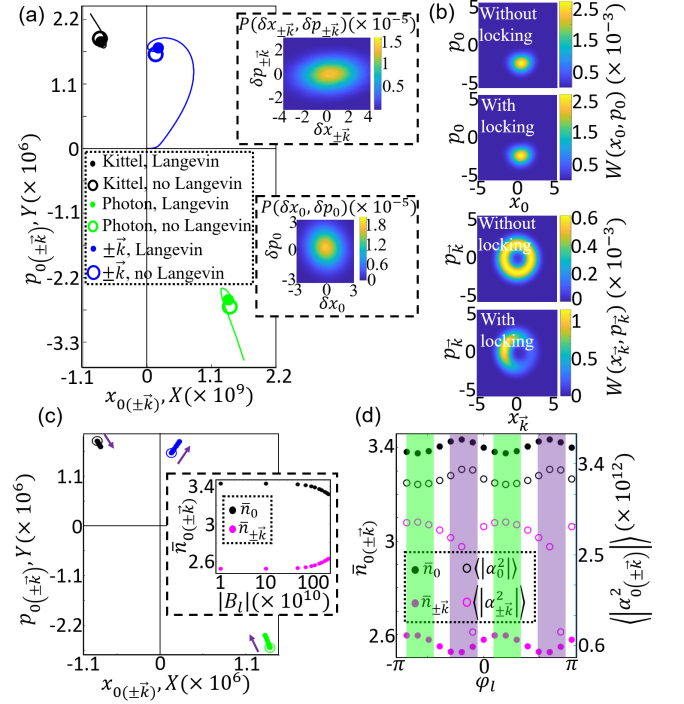


FIG. 7. Injection locking of $\pm\vec{k}$ modes calculated by (a) the Langevin formalism and (b) the quantum master equation at the (ω_0, ω_d) of the black star in Fig. 2. (a) Main panel: The averaged trajectories from the initial to the final states (filled dots) for all modes. $|B_l| = 10^{12} \text{ 1/s}$ ($< \bar{B}/10$). The color code explained in the panel is applicable also to (c). Insets: Probability distributions of the fluctuations. The final states from entirely classical calculations and without injection locking are also shown. (b) Results from the quantum master equation, without and with injection locking as indicated. (c) Main panel (Langevin): the averaged final states of all fields as a function of locking field B_l from 10^{10} to $2 \times 10^{12} \text{ s}^{-1}$ with fixed $\phi_l = 0$. The purple vectors indicate the shift direction with increasing B_l . Inset: Mean magnon number $\bar{n}_{0(\pm\vec{k})}$ in the scaled quantum system as a function of B_l with $\phi_l = 0$. (d) Dependence of the averaged $|\alpha_{0(\pm\vec{k})}|^2$ for the final states from Langevin (right axis) and $\bar{n}_{0(\pm\vec{k})}$ from quantum master equation calculations (left axis), on the phase $\phi_l \in \{-\pi, \pi\}$ for a fixed $|B_l| = 10^{12} \text{ s}^{-1}$. The purple (green) colored background emphasizes ϕ_l values with weak (strong) locking.

Kittel mode magnons and photons decrease. The effects are small but establish identical trends in both Langevin and quantum formalisms. According to Fig. 7(d), the phase ϕ_l modulates the excitations with periodicity of π , since the force is proportional to $\cos(\phi_l + \phi_0)$, where ϕ_0 is a constant shift [24]. Strong (weak) locking implies larger (smaller) number of $\pm\vec{k}$ magnons, and smaller (larger) number of Kittel mode magnons and photons both in Fig. 7(c) and (d): The mean magnon numbers $\bar{n}_{0(\pm\vec{k})}$ in the scaled quantum system follow the trends of the equivalent $|\alpha_{0(\pm\vec{k})}|^2$ of the Langevin formalism.

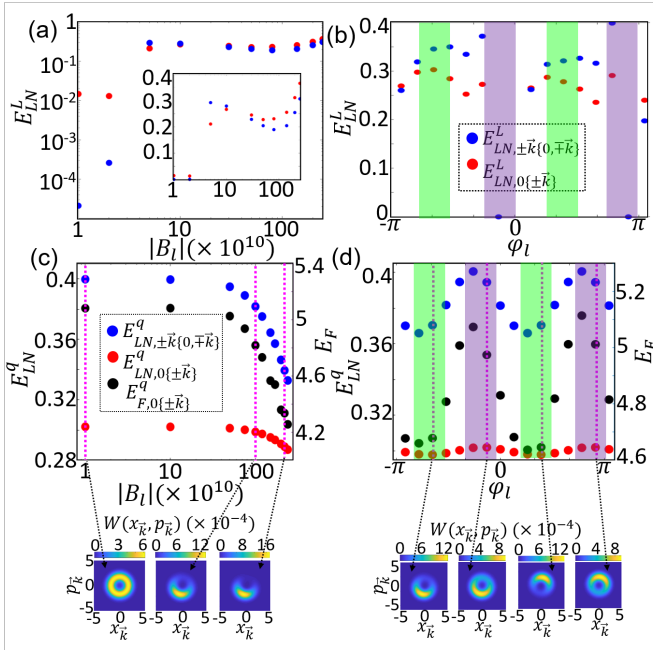


FIG. 8. Entanglement in an excited magnon system with injection locking. (a) The logarithmic negativity E_{LN}^L of steady states from the Langevin formalism as a function of $|B_l|$ for $\phi_l = 0$. In the main panel, both axes are on a log scale. The inset contains the same data on a linear scale. (b) E_{LN}^L as a function of ϕ_l , at $|B_l| = 10^{12} \text{ s}^{-1}$. (c) and (d) Logarithmic negativities (left axis) $E_{LN,0\pm\vec{k}}^q$, $E_{LN,\pm\vec{k},0\mp\vec{k}}^q$, and entanglement of formation (right axis) $E_{F,0\pm\vec{k}}^q$, in the steady state, calculated by the quantum master equation as a function of $|B_l|$ for $\phi_l = 0$ and as a function of ϕ_l for $|B_l| = 10^{12} \text{ s}^{-1}$, respectively. Bottom insets of (c) and (d) are Wigner functions of $\pm\vec{k}$ modes for particular values of $|B_l|$ and ϕ_l , respectively, indicated by black dashed arrows and purple dashed lines. In (b) and (d), the purple (green) colored bars indicate ϕ_l values corresponding to weak (strong) locking.

B. Injection locking and Gaussian distillable entanglement

The beneficial effects of locking on the logarithmic negativity extracted from the semi-classical covariance matrix for continuous variable entanglement as a function of $|B_l|$ and ϕ_l are evident in Figs. 8(a) and 8(b). Figure 8(a) shows that both $E_{LN,0\pm\vec{k}}^L$ and $E_{LN,\pm\vec{k},0\mp\vec{k}}^L$ become nonzero by increasing $|B_l|$ to values where locking is achieved and reach ~ 0.3 , which is in the range of the predicted E_{LN}^q without injection locking. Therefore, the distillable entanglement became that of continuous variables and is accessible from the covariance matrix. Figure 8(b) shows that $E_{LN,0\pm\vec{k}}^L$ ($E_{LN,\pm\vec{k},0\mp\vec{k}}^L$) strongly depends on the phase ϕ_l . For the ϕ_l with weakest locking, $E_{LN}^L = 0$.

C. Effect of injection locking on entanglement

As mentioned earlier, in contrast to the general one, continuous-variable bipartite entanglement requires injection locking. We assess the former by studying the density matrix of the scaled system that solves the quantum master equation, using the logarithmic negativity and entanglement of formation E_F . The entanglement of formation E_F [79, 80] in the bipartite configuration (i) is calculated by the algorithm [81] explained in Appendix D 2. It should be noted that for a mixed state E_F can be very different from (but always larger than) the distillable entanglement [80, 82]. Figures 8(c) and (d) show the dependence of $E_{LN,0\pm\vec{k}}^q$, $E_{LN,\pm\vec{k},0\mp\vec{k}}^q$, and $E_{F,0\pm\vec{k}}^q$ on locking field amplitude $|B_l|$ and phase ϕ_l . All entanglement measures are nonzero without the injection locking, and remain finite when locking is added. However, a stronger locking somewhat reduces $E_{LN,0\pm\vec{k}}^q$, $E_{LN,\pm\vec{k},0\mp\vec{k}}^q$, and E_F , in contrast to $E_{LN,0\pm\vec{k}}^L$, $E_{LN,\pm\vec{k},0\mp\vec{k}}^L$, which are strongly enhanced by it. At large locking amplitudes $E_{LN}^q \approx E_{LN}^L$, as expected for Gaussian states. The colored background in Figs. 8(b) and (d) codes the regions with stronger (green) and weaker (purple) effects of locking. In particular, Wigner functions of the $\pm\vec{k}$ modes in Figs. 8(c) and (d), display more ring-like (coherent state) features, which explain weaker (stronger) effects of locking. Phase-locking the existing $\pm\vec{k}$ magnons induces a fraction of magnons on top of those generated by the instability of the Kittel mode, since they are driven by both $i(B_l e^{-i\omega_L t} c_{\pm\vec{k}}^\dagger - B_l^* e^{i\omega_L t} c_{\pm\vec{k}})$ and the (mean-field) 4MS term $\mathcal{D}_{0,\vec{k}}^{4MS,2} \alpha_0^2 \alpha_{\pm\vec{k}} c_{\mp\vec{k}} + \text{h.c.}$ (see Appendix A). $\mathcal{D}_{0,\vec{k}}^{4MS,2} \alpha_0^2 \alpha_{\pm\vec{k}} \sim 10^{12} \text{ s}^{-1}$ has the same order of magnitude as B_l' . Stronger locking reduces the number of magnons paired with the Kittel mode magnons (i.e. generated from 4MS terms), and therefore the entanglement measures E_{LN}^q and E_F as observed in Figs. 8(c) and 8(d). We compare the dependence of E_{LN}^L and E_{LN}^q on ϕ_l in Figs. 8(b) and 8(d). E_{LN}^L (E_{LN}^q) is larger (smaller) for ϕ_l corresponding to stronger (weaker) locking, even vanishes at some phase angles for which the limit cycle is not significantly suppressed. The inequality $E_F \geq E_{LN}$ is always obeyed.

VII. EXPERIMENTAL RELEVANCE

The injection locking Hamiltonian and distillation of the entanglement requires coupling of an AC magnetic field to the $\pm\vec{k}$ magnons, i.e., a spatial modulation in the dynamic magnetization with period $\sim \lambda_{\pm\vec{k}} = 2\pi/k \sim 100 \text{ nm}$, which can be accomplished by gratings such as a periodically modulated coplanar waveguide close to either sphere or thin film [Figs. 9(a) and 9(b)], periodic trenches in a YIG thin film [Fig. 9(c)] [32], or a 2D ferro-

magnetic nanowire array deposited on top of a thin film [Fig. 9(d)] [83]. In Fig. 9(d), nano-structured magnets act as in-phase antenna for the microwave input at frequency $\omega_{\pm\vec{k}}$ [83]. For a sphere, a periodic waveguide [Figs. 9(a) and 9(b)] appears to be the only viable method, but microwave fields lose their modulation with distance. The quality of the spatial modulation improves with reduced size of the sphere to say tens of μm . The k value of interest is not affected by the size of the magnetic element down to a radius of $> 1\mu\text{m}$, and therefore the periods in the proposed structures in Figs. 9(a)-(d) do not have to be scaled. The parameters of the staggered waveguide in Figs. 9(a) and (b) are the signal wire width W_s and the width of the gap between signal and ground lines W_g . Figure 9(b) also shows a snapshot of the AC magnetic field $\vec{B}_{wg} = B_{wg}^x \hat{x} + B_{wg}^y \hat{y}$ [84], for $W_s = W_g = 10\text{ nm}$ and input voltage $V_{wg} = 10\text{ mV}$, which governs B_l as a function of the waveguide input power $P_{in,wg}$. It is periodic in z with wave length $\lambda_{\pm\vec{k}}$. Here B_{wg}^x may be disregarded because the integral of $B_{wg}^x m_{\pm\vec{k}}^x$ vanishes, where $m_{\pm\vec{k}}^x(x, y)$ is a magnetization of a volume mode with $\vec{k} \parallel \hat{z}$. On the other hand, B_{wg}^y has finite overlap with $m_{\pm\vec{k}}^y(x, y)$ since modulated by the same wavelength. We can quench an unwanted coupling to the Kittel mode by a $\pi/2$ phase shift of the input power between the two waveguides. For a cube with $V_m = (100\mu\text{m})^3$, we chose $\bar{B} \sim 10^{13}\text{ s}^{-1}$ and $B_l = \gamma\sqrt{M_s V_m}/\gamma\hbar B_{wg}^y = 10^{12}\text{ s}^{-1}$ where average B_{wg}^y over the magnet $B_{wg}^y \sim 0.2\text{ mT}$. Based on the field distribution B_{wg}^y in Fig. 9(b) which is for $V_{wg} = 10\text{ mV}$, a simple approximation shows that the required B_{wg}^y is thus obtained using $V_{wg} = \sqrt{2P_{in,wg}Z_0} = 0.1\text{ V}$ or a waveguide input drive power $P_{in,wg} \sim 0.1\text{ mW}$ and impedance $Z_0 \sim 50\Omega$. For a $10\mu\text{m}$ cube, $V_{wg} = \sqrt{2P_{in,wg}Z_0} = 1\text{ mV}$ or a waveguide input drive power $P_{in,wg} \sim 10\text{ nW}$ is adequate to provide the required $B_l \sim 10^{11}\text{ 1/s}$. This is a small perturbation on top of the cavity drive, which for $V_m = (10\mu\text{m})^3$ is $P_{in} = 10\mu\text{W}$ corresponding to $\bar{B} \sim 10^{12}\text{ 1/s}$.

The microwaves that drive magnons out of equilibrium, heat the magnetic system by Gilbert damping to temperatures above the assumed $T_{\text{env}} \sim 1\text{ K}$, so we have to assess the conditions at which our theory remains applicable. Let us assume a lattice temperature of the magnet of T_L and an environmental one T_{env} . We assume that the magnet is in contact with an acoustically matched material such as gadolinium gallium garnet (GGG) with temperature equal to T_L at the contact to YIG and T_S at the other side, which can be kept lower than T_{env} if actively cooled. Geometrically, we assume a sample which is narrow and suddenly becomes wide. The wide part of the sample is the magnetic cube kept at T_L and there is a gradient in the narrow one, GGG substrate. In the steady state, the power input P_G by Gilbert damping must equal the heat current through the substrate $P_G = G_{\text{GGG}}(T_L - T_S)$, where the heat conductance $G_{\text{GGG}} = \sigma_{\text{GGG}}d_{\text{GGG}}$, with thermal conductivity $\sigma_{\text{GGG}} \sim 7\text{ W/(K}\cdot\text{m)}$ [85] and d_{GGG}

is the thickness of the substrate. $P_G = \hbar\omega_0|\alpha_0|^2\zeta_{m,0}$, where $\zeta_{m,0}$ is the Kittel magnon dissipation rate [86]. A magnon number $|\alpha_0|^2$ less than 10^{14} [see e.g. Fig. 1(c)] causes $P_G \sim 10^{-3}\text{ W}$. Therefore the heat sink temperature should be kept at $T_S \sim T_L - (d_{\text{GGG}}/1\text{ mm})\text{ K}$. For a smaller magnet with $10\mu\text{m}$ dimension, $P_G \sim 10^{-6}\text{ W}$ and for $d_{\text{GGG}} \sim 1\mu\text{m}$, $T_S \sim 0.9\text{ K}$ is adequate to keep $T_L \sim 1\text{ K}$. A magnetic sphere attached to the cooling system by a glue may face a higher heat resistance to the heat sink. The same statement applies to the resistance of the interface of the heat sink and the environment. The relevant parameter is then the total interface heat conductance of the magnet with environment. The worst case scenario corresponds to the magnetic sphere (cube) free standing in the environment (no heat sink), and $P/S_M = G_{LE}(T_L - T_{\text{env}})$ is applicable, where S_M is the surface of the magnet, and G_{LE} is the effective interface thermal conductance of magnet lattice/environment interface. When T_{env} is in tens of mK regime and magnet dimension is $10\mu\text{m}$, $G_{LE} \sim 10^4\text{ W/Km}^2$ is adequate to keep $T_L \sim 1\text{ K}$, which can be achieved in cryogenic environments [87]. In presence of heat sink, conditions are more relaxed, i.e. smaller (larger) G_{LE} (T_{env}) can still lead to desired $T_L \sim 1\text{ K}$.

Finally, we address the observability of the predicted entanglement in the set-ups of Figure 9. The input drive to the cavity and the waveguide should be locked by a tunable phase shifter for the waveguide input. The output cavity field contains the information on the amplitude and squeezing of the Kittel mode (see Fig. 5). The waveguide output reveals essential information about the statistics of the $\pm\vec{k}$ pairs, e.g. the limit-cycle attractors [see Fig. 3(a)] and in the case of injection-locking, fixed-point dynamics (see Fig. 7). Both outputs are required to detect bipartite entanglement of the Kittel mode and the $\pm\vec{k}$ pair. Figure 9(d) illustrates the homodyne tomography [66] method implemented in [88, 89]. The balanced homodyne detection (BHD) output X' determines the quadrature statistics of the input signal by varying the phase of the local oscillator (LO) and measuring X' many times to reveal its first and second moments [64, 66]. For example, the BHD detection of the cavity field characterizes X' as a function of LO phase, which leads to the Wigner functions of Fig. 5(c). For bipartite entanglement, the corresponding covariance matrix should be evaluated, which consists of two diagonal and two off-diagonal blocks. The former are evaluated by feeding either the output of the cavity b_{out} or the output of the waveguide b'_{out} to the BHD. For the off-diagonal blocks, the feed should be $b_1 = (b_{\text{out}} + ib'_{\text{out}})/\sqrt{2}$, $b_2 = (b_{\text{out}} - b'_{\text{out}})/\sqrt{2}$, and $b_3 = (b_{\text{out}} + b'_{\text{out}})/\sqrt{2}$ [88], while both quadrature statistics should be evaluated. The fields b_1 , b_2 , and b_3 can be filtered out by phase shifters and mixing at beamsplitters, as depicted in Fig. 9(e). From the covariance matrix elements, $E_{LN,0\pm\vec{k}}$ can be extracted.

The sketched quantum state tomography is a main-

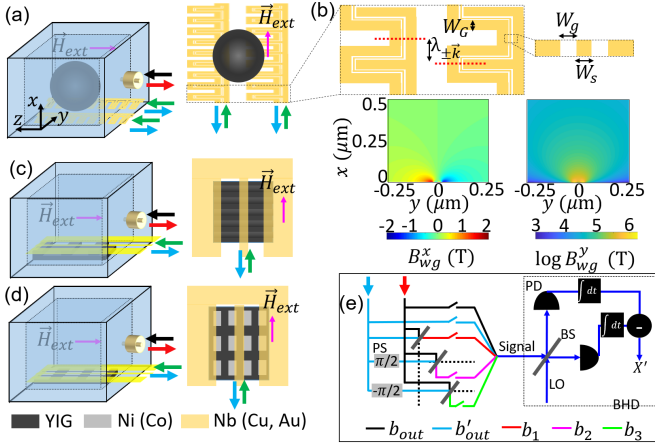


FIG. 9. Proposed set-ups to measure entanglement in magnets. (a), (c) and (d) A magnetic sphere or film in a rectangular cavity with wave guides for injection locking. The black and red arrows indicate the input drive \vec{B} and output microwave fields (b_{out}), respectively. The green arrows are the locking field B_l applied by a coplanar waveguide and the blue arrow is the corresponding output signal (b'_{out}). The suggested materials for (a), (c) and (d) are indicated at the bottom of panel (d). (b) Top panel: Zoom-in of a section of the staggered waveguide in (a), and the dimensions W_G , $\lambda_{\pm\vec{k}}$, W_g , and W_s . Bottom panel: Magnetic field distribution along either of the red dashed lines in the top panel, for $W_s = W_g = 10$ nm and voltage $V_{wg} = 10^{-2}$ V. (e) Equivalent electronic circuit model including beam splitters (BS), phase ($\pm\pi/2$) shifters (PS), switches, photon number detectors (PD), temporal integrators (indicated by $\int dt$), a subtractor [indicated by $(-)$], signal and local oscillator (LO) lines. The color code of the signal lines is given in the bottom of the panel. The dashed black lines are unused signals. The output X' is governed by the LO-phase, while the signal line forms the input to the homodyne detection (the parts enclosed by the dashed black rectangle).

stream technique for quantum information studies with light. The large photon energy renders single photon detection relatively easy. Similar experiments in the microwave regime have been carried out only recently [90–92]. Standard microwave components such as high electron mobility transistors and linear detectors, as well as proper design of beam splitters [93, 94] led to development of techniques suitable for microwave quantum state tomography. These techniques demonstrated and characterized path entanglement [92], as is required to test our predictions.

VIII. CONCLUSION

Quantum information and its resources such as squeezing and entanglement have been pursued for discrete variables [95], continuous variables in position-momentum phase space [67], and continuous variables on the Bloch sphere phase space [96]. Both discrete and continuous

variable systems have been considered for quantum computation [97, 98], while squeezed and entangled photons or magnons [67, 99] displayed sub-shot noise and quantum teleportation [100, 101]. Non-classicalities in continuous variables [42, 102, 103] pave the way for future quantum computation protocols [104]. Therefore, continuous variable quantum information offers more opportunities than that with discrete variables, simply because the accessible Hilbert space is larger. Here, we uncovered the continuous variable quantum information resources of a coherently driven magnet, promising a large steady-state deterministic entanglement by virtue of the nonlinearities and anisotropies of the magnetization dynamics. For that reason we believe that magnons can beat alternative systems such as mechanical membranes and cantilevers coupled to cavity photons [40] as squeezing and entanglement resources. The GHz magnons in our scheme are strongly entangled in magnets down to the micrometer regimes, which is difficult to achieve in mechanical systems. The scalability could help profit from the flexibility of artificial metamaterials, such as arrays of N nanomagnets on top of a waveguide [see e.g. Fig. 9(a)], thereby accessing a large amount of deterministic bipartite entangled states ($\sim 0.3 \times N$). More theoretical and experimental efforts to utilize magnets in quantum information are needed, however. The viscous damping of the magnetization dynamics is larger than that of other systems. While this is of little direct concern for coherently driven systems, the associated temperature increase must be controlled by advanced heat management. Nanostructuring of high quality magnets is required, but still in its infancy [55].

Another direction to be pursued is based on treating the magnetostatic manifold as atomic levels and assess quantum information resources on Bloch spheres corresponding to two such levels. The latter can provide a link to laser induced spin-orbit coupling [105, 106] of magnons and topology in a single magnet. Moreover, the inherent chirality of magnon-photon coupling [107] can be employed to achieve light induced spin-orbit coupling of magnons in more than one magnet and magnonic lattices with controllable topology [106]. These would allow topological quantum information protocols [108] or unique features such as robustness of edge states, and conventional quantum information as addressed in this paper, coexisting in a single magnet or a collection of them [109].

ACKNOWLEDGMENTS

This work is financially supported by JSPS KAKENHI (Grant No. 19H006450) and the Nederlandse Organisatie voor Wetenschappelijk Onderzoek (NWO). M. E. conducted part of this research at Kavli Institute of Nanoscience, Delft University of Technology. During part of this research, M. E. was supported by Postdoctoral Fellowship of Japan Society for Promotion of Science (JSPS)

for overseas researchers and JSPS KAKENHI (Grant No. 16F16325).

Appendix A: Hamiltonian

This section reviews well-known results and defines our notation [16, 22, 47, 53]. The external magnetic field and equilibrium magnetization are along \hat{z} .

Dipolar interaction: The (time-dependent) dipolar (Zeeman) interaction reads

$$H^{(d)} = -\frac{\mu_0}{2} \int \vec{m}(\vec{r}) \cdot \vec{h}^{(d)}(\vec{r}) d\vec{r}, \quad (A1)$$

where μ_0 is the vacuum permeability, $\vec{h}^{(d)}$ is the dipolar field and \vec{m} is the magnetization texture in real space. $H^{(d)}$ for a bulk magnet can be derived from a Heisenberg Hamiltonian for a lattice of N cells with spin S by the Holstein-Primakoff (HP) transformation. Internal excitations of large spins in materials such as YIG with local moment $S = 5/2$ start to play a role only when the local spin excitation exceeds \hbar or $n_0/(NS) \gtrsim 0.1$. We operate here at ~ 1 K, so $n_0/(NS) \lesssim 0.01$, which implies that the simple Holstein-Primakoff expansion is valid. The magnetization vector $\vec{m}_{\vec{k}}$ in Fourier space can then be written in terms of the magnon annihilation (creation) field operators $a_{\vec{k}}$ ($a_{\vec{k}}^\dagger$). To third order in field operators

$$\begin{aligned} \mathbf{m}_{x,\vec{k}} &= \hbar\gamma \left(\frac{NS}{2V} \right)^{\frac{1}{2}} (a_{\vec{k}} + a_{-\vec{k}}^\dagger) - \hbar\gamma \left(\frac{\hbar\gamma}{32M_s V^2} \right)^{\frac{1}{2}} \\ &\quad \left(\sum_{\vec{k}_1, \vec{k}_2} a_{\vec{k}_1}^\dagger a_{\vec{k}_2}^\dagger a_{\vec{k}+\vec{k}_1+\vec{k}_2} + a_{\vec{k}_1} a_{\vec{k}_2} a_{-\vec{k}+\vec{k}_1+\vec{k}_2}^\dagger \right), \\ \mathbf{m}_{y,\vec{k}} &= -i\hbar\gamma \left(\frac{NS}{2V} \right)^{\frac{1}{2}} (a_{\vec{k}} - a_{-\vec{k}}^\dagger) + i\hbar\gamma \left(\frac{\hbar\gamma}{32M_s V^2} \right)^{\frac{1}{2}} \\ &\quad \left(\sum_{\vec{k}_1, \vec{k}_2} a_{\vec{k}_1}^\dagger a_{\vec{k}_2}^\dagger a_{\vec{k}+\vec{k}_1+\vec{k}_2} - a_{\vec{k}_1} a_{\vec{k}_2} a_{-\vec{k}+\vec{k}_1+\vec{k}_2}^\dagger \right), \\ \mathbf{m}_{z,\vec{k}} &= M_s \sqrt{V} - \frac{\gamma\hbar}{\sqrt{V}} \sum_{\vec{k}_1} a_{-\vec{k}_1}^\dagger a_{\vec{k}-\vec{k}_1}, \end{aligned} \quad (A2)$$

where $M_s = g\mu_B NS/V$ is the saturation magnetization, V is the volume of the sample, g is the electron g-factor, and μ_B is the Bohr magneton.

When k^{-1} , with $k = |\vec{k}|$, approaches the sample dimensions, the spectrum becomes a discrete manifold of magnetostatic modes. For the uniform mode

$$\vec{h}^{(d),(0)} = \left(-N_x \mathbf{m}_{x,\vec{k}=0} \hat{x} - N_y \mathbf{m}_{y,\vec{k}=0} \hat{y} - N_z \mathbf{m}_{z,\vec{k}=0} \hat{z} \right), \quad (A3)$$

where for a sphere the demagnetizing constants $N_{x(y,z)} = 1/3$, while for a thin film, $N_x = N_y = 0$ and $N_z = 1$. For large enough k , the magnons in a sphere are well described by plane waves and a continuous spectrum. Their

dipolar field reads

$$\vec{h}^{(d)} = - \sum_{\vec{k} \neq 0} \hat{k} \left(\hat{k} \cdot \vec{m}_{\vec{k}} \right), \quad (A4)$$

Following Suhl [53], we use Eq. (A4) for all $\vec{k} \neq 0$ when computing magnon interactions. The dipolar interaction Hamiltonian Eqs. (A1), (A3) and (A4) can then be written as a sum of several terms involving the Kittel mode $\delta_{\vec{k},0}$ and plane spin wave (PW) modes $1 - \delta_{\vec{k},0}$,

$$\begin{aligned} H^{(d)} &= \sum_{\vec{k}} \frac{1}{2} \left\{ \left[\frac{|k_+|^2}{2k^2} \mathbf{g}^2 (1 - \delta_{\vec{k},0}) \right] a_{\vec{k}}^\dagger a_{\vec{k}} \right. \\ &\quad + \left(N_T' \mathbf{g}^2 \delta_{\vec{k},0} - 2N_z \mathbf{g}'' \mathbf{g}''' \right) a_{\vec{k}}^\dagger a_{\vec{k}} \\ &\quad + \left(\left[\frac{k_+^2}{4k^2} \mathbf{g}^2 (1 - \delta_{\vec{k},0}) + \frac{N_T}{2} \mathbf{g}^2 \delta_{\vec{k},0} \right] a_{\vec{k}}^\dagger a_{-\vec{k}}^\dagger + \text{H.c.} \right) \\ &\quad + \sum_{\vec{k}'} \left(\left[\frac{-k_+ k_z}{2k^2} \mathbf{g} \mathbf{g}''' (1 - \delta_{\vec{k},0}) \right] a_{\vec{k}}^\dagger a_{\vec{k}'}^\dagger a_{\vec{k}+\vec{k}'} + \text{H.c.} \right) \\ &\quad + \sum_{\vec{k}', \vec{k}''} \left(\left[\frac{k_z^2}{k^2} \mathbf{g}'''^2 (1 - \delta_{\vec{k},0}) \right] a_{\vec{k}}^\dagger a_{\vec{k}'}^\dagger a_{\vec{k}+\vec{k}'} a_{-\vec{k}+\vec{k}''} \right) \\ &\quad - \sum_{\vec{k}', \vec{k}''} \left(N_T \mathbf{g} \mathbf{g}' \delta_{\vec{k},0} a_0^\dagger a_{\vec{k}+\vec{k}'}^\dagger a_{\vec{k}} a_{\vec{k}''} + \text{H.c.} \right) \\ &\quad - \sum_{\vec{k}', \vec{k}''} \left\{ \left[\frac{k_-^2}{k^2} \mathbf{g} \mathbf{g}' (1 - \delta_{\vec{k},0}) \right] a_{\vec{k}}^\dagger a_{\vec{k}'}^\dagger a_{\vec{k}} a_{-\vec{k}+\vec{k}'+\vec{k}''} + \text{H.c.} \right\} \\ &\quad \left. + N_z \mathbf{g}'''^2 \delta_{\vec{k},0} \sum_{\vec{k}', \vec{k}''} a_{\vec{k}'}^\dagger a_{\vec{k}''}^\dagger a_{\vec{k}} a_{\vec{k}'} \right\}, \end{aligned} \quad (A5)$$

where $\mathbf{g} = \sqrt{2\hbar\mu_0\gamma M_s}$, $\mathbf{g}' = \hbar\gamma\sqrt{\hbar\mu_0\gamma/(32M_s V^2)}$, $\mathbf{g}'' = M_s\sqrt{\mu_0 V}$, $\mathbf{g}''' = \hbar\gamma\sqrt{\mu_0/V}$, $k_\pm = k_x \pm ik_y$, $2N_T = N_x - N_y$, $2N_T' = N_x + N_y$. In this notation, in order to conserve the units γ values should be input in units of $1/(\text{T} \cdot \text{s})$.

Exchange interaction: The exchange Hamiltonian in real space $H^{(exc)} = \mu_0 \mathcal{E} / (2M_s V) \int (\nabla \vec{m}(\vec{r}))^2 d\vec{r}$, where \mathcal{E} is the exchange constant. In momentum space $H^{(exc)} = \mu_0 \mathcal{E} / (2M_s) \sum_{\vec{k}, \vec{k}'} k^2 \vec{m}_{\vec{k}} \cdot \vec{m}_{\vec{k}'}$, which leads to

$$\begin{aligned} H^{(exc)} &= \\ &\sum_{\vec{k} \neq 0} k^2 \frac{\mathcal{E}}{2M_s} \left\{ \mathbf{g}^2 a_{\vec{k}}^\dagger a_{\vec{k}} + \mathbf{g}'''^2 \sum_{\vec{k}', \vec{k}''} \left(a_{\vec{k}'}^\dagger a_{\vec{k}''}^\dagger a_{\vec{k}+\vec{k}'} a_{-\vec{k}+\vec{k}''} \right) \right\}. \end{aligned} \quad (A6)$$

Crystalline anisotropy: The crystalline magnetic anisotropy energy $H^{(A)} = -\mu_0 \vec{m} \cdot \vec{N}_A \vec{m}$ in terms of the anisotropy tensor \vec{N}_A . We assume here easy-axis or easy-plane anisotropy with crystal symmetry axis along \vec{M}_0 . \vec{N}_A is then diagonal with elements $N_{A,x(y,z)}$ and can be classified in terms of symmetric ($2N_{A,s} = N_{A,x} + N_{A,y}$),

antisymmetric ($2N_{A,as} = N_{A,x} - N_{A,y}$), and ($N_{A,z}$) components, leading to

$$H^{(A)} = - \sum_{\vec{k}} \frac{1}{2} \left\{ (\mathbf{g}^2 N_{A,s} - 2\mathbf{g}''\mathbf{g}''' N_{A,z}) a_{\vec{k}}^\dagger a_{\vec{k}} + \frac{\mathbf{g}^2}{2} N_{A,as} (a_{\vec{k}}^\dagger a_{-\vec{k}}^\dagger + a_{\vec{k}} a_{-\vec{k}}) - \sum_{\vec{k}', \vec{k}''} N_{A,as} (2\mathbf{g}\mathbf{g}' a_{\vec{k}}^\dagger a_{\vec{k}'}^\dagger a_{\vec{k}+\vec{k}''} a_{-\vec{k}-\vec{k}''} + H.c.) + \sum_{\vec{k}', \vec{k}''} N_{A,z} (\mathbf{g}'''^2 a_{\vec{k}}^\dagger a_{\vec{k}'}^\dagger a_{\vec{k}+\vec{k}''} a_{-\vec{k}-\vec{k}''}) \right\}. \quad (\text{A7})$$

The first term $\frac{1}{2} (\mathbf{g}^2 N_{A,s} - 2\mathbf{g}''\mathbf{g}''' N_{A,z}) a_{\vec{k}}^\dagger a_{\vec{k}}$ causes only a small constant shift of the dispersion that may be disregarded. In a cubic crystal, when $\vec{M}_0 \parallel [001]$, $N_{A,s} \neq 0$ and $N_{A,as} = N_z = 0$ [16, 56], while for $\vec{M}_0 \parallel [111]$, $N_{A,s} = N_{A,as} = 0$ and $N_{A,z} \neq 0$. When $\vec{M}_0 \parallel [110]$, $N_{A,s} \approx 3N_{A,as}$, and $N_{A,z} \approx 2N_{A,as}$, the crystal anisotropy affects the Kittel mode besides a constant shift by $\mathbf{g}^2 N_{A,as} (a_0^\dagger a_0^\dagger + a_0 a_0)/2$, again to lowest (bilinear) order in the field operators.

Zeeman interaction: The Zeeman energy of an applied magnetic field $\vec{H}_{ext} = H_{ext} \hat{z} \parallel \vec{M}_0$

$$H^{(Z)} = \hbar\gamma\mu_0 H_{ext} \sum_{\vec{k}} a_{\vec{k}}^\dagger a_{\vec{k}} \quad (\text{A8})$$

depends only on the total number of magnons.

Total magnetic Hamiltonian: Collecting Eqs. (A5-A8), the total Hamiltonian becomes $H^{(T,m)} = \sum_{\vec{k}} H_{\vec{k}}^{(T,m)}$ with

$$H_{\vec{k}}^{(T,m)} = \mathcal{A}_{\vec{k}} a_{\vec{k}}^\dagger a_{\vec{k}} + \left[\mathcal{B}_{\vec{k}} a_{-\vec{k}}^\dagger a_{\vec{k}}^\dagger + H.c. \right] + \sum_{\vec{k}'} \left[\mathcal{C}_{\vec{k}} a_{\vec{k}}^\dagger a_{\vec{k}'}^\dagger a_{\vec{k}+\vec{k}'} + H.c. \right] + \sum_{\vec{k}', \vec{k}''} \left[\mathcal{D}_{\vec{k}} a_{\vec{k}}^\dagger a_{\vec{k}'}^\dagger a_{\vec{k}+\vec{k}'+\vec{k}''} a_{-\vec{k}-\vec{k}''} + H.c. \right] + \sum_{\vec{k}', \vec{k}''} \left[\mathcal{D}'_{\vec{k}} a_{\vec{k}}^\dagger a_{\vec{k}'}^\dagger a_{\vec{k}+\vec{k}'} a_{-\vec{k}-\vec{k}''} \right], \quad (\text{A9})$$

and matrix elements

$$\mathcal{A}_{\vec{k}} = \frac{|k_+|^2 g^2}{4k^2} (1 - \delta_{k,0}) + \frac{1}{2} N_T' \mathbf{g}^2 \delta_{k,0} - N_z \mathbf{g}'' \mathbf{g}''' \quad (\text{A10})$$

$$\mathcal{B}_{\vec{k}} = \frac{k_+^2 g^2}{8k^2} (1 - \delta_{k,0}) + \frac{N_T \mathbf{g}^2}{4} \delta_{k,0} - \frac{\mathbf{g}^2}{4} N_{A,as}, \quad (\text{A11})$$

$$\mathcal{C}_{\vec{k}} = -\frac{k_+ k_z g g'''}{4k^2} (1 - \delta_{k,0}), \quad (\text{A12})$$

$$\mathcal{D}_{\vec{k}} = -\frac{k_-^2 g g'}{2k^2} (1 - \delta_{k,0}) - \frac{1}{2} N_T g g' \delta_{k,0} + g g' N_{A,as}, \quad (\text{A13})$$

$$\mathcal{D}'_{\vec{k}} = \frac{k_z^2 \mathbf{g}'''^2}{2k^2} (1 - \delta_{k,0}) + \frac{1}{2} N_z \mathbf{g}'''^2 \delta_{k,0} - \frac{1}{2} N_{A,z} \mathbf{g}'''^2 + \frac{k_-^2 \mathcal{E} \mathbf{g}'''^2}{2M_s}, \quad (\text{A14})$$

The term $\mathcal{B}_{\vec{k}} a_{-\vec{k}}^\dagger a_{\vec{k}}^\dagger + H.c.$ in Eq. (A9) is diagonalized by the Bogoliubov transformation

$$a_{\vec{k}} = u_{\vec{k}} c_{\vec{k}} - v_{\vec{k}} c_{-\vec{k}}^\dagger, \quad a_{\vec{k}}^\dagger = u_{\vec{k}}^* c_{\vec{k}}^\dagger - v_{\vec{k}}^* c_{-\vec{k}}, \quad (\text{A15})$$

with

$$u_{\vec{k}} = \left(\frac{\mathcal{A}_{\vec{k}} + \omega_{\vec{k}}}{2\omega_{\vec{k}}} \right)^{\frac{1}{2}}; v_{\vec{k}} = \frac{\mathcal{B}_{\vec{k}}}{|\mathcal{B}_{\vec{k}}|} \left(\frac{\mathcal{A}_{\vec{k}} - \omega_{\vec{k}}}{2\omega_{\vec{k}}} \right)^{\frac{1}{2}}, \quad (\text{A16})$$

and $\omega_{\vec{k}} = \sqrt{\mathcal{A}_{\vec{k}}^2 - |\mathcal{B}_{\vec{k}}|^2}$. The quadratic terms in $H^{(T,m)}$ in Eq. (A9) reduce to the harmonic oscillator $\omega_{\vec{k}} c_{\vec{k}}^\dagger c_{\vec{k}}$.

After some algebra, the three magnon terms in the second line of Eq. (A9) may be transformed and simplified to

$$H^{(3MS)} = \sum_{\vec{k}} \left(\mathcal{C}_{\vec{k}}^{(3MS)} c_0 c_{\vec{k}}^\dagger c_{-\vec{k}}^\dagger + H.c. \right),$$

where

$$\mathcal{C}_{\vec{k}}^{(3MS)} = \left[\mathcal{C}_{\vec{k}} \left(u_{\vec{k}}^* v_{\vec{k}}^* v_{\vec{k}} + |u_{\vec{k}}|^2 u_0 \right) + \mathcal{C}_{\vec{k}}^* \left(-v_{\vec{k}} u_0 u_{\vec{k}}^* - |v_{\vec{k}}|^2 v_0^* \right) \right]. \quad (\text{A17})$$

The four-magnon scattering terms are transformed into $H^{(4MS)} = \sum_{\vec{k}, \vec{k}', \vec{k}''} \left(H_{\vec{k}, \vec{k}', \vec{k}''}^{(4MS,1)} + H_{\vec{k}, \vec{k}', \vec{k}''}^{(4MS,2)} \right)$, where $H_{\vec{k}, \vec{k}', \vec{k}''}^{(4MS,1)}$ corresponds to the third line of Eq. (A9), while $H_{\vec{k}, \vec{k}', \vec{k}''}^{(4MS,2)}$ corresponds to the fourth line of Eq. (A9). Keeping only the combinations that can satisfy resonant conditions leads to the simplified

$$H^{(4MS)} = \sum_{\vec{k}, \vec{k}'} \left[\left(\mathcal{D}_{\vec{k}, \vec{k}'}^{4MS,1} c_{\vec{k}}^\dagger c_{\vec{k}}^\dagger c_{\vec{k}'}^\dagger c_{\vec{k}'} + \mathcal{D}_{\vec{k}, \vec{k}'}^{4MS,2} c_{\vec{k}}^\dagger c_{-\vec{k}}^\dagger c_{\vec{k}'} c_{-\vec{k}'} \right) + H.c. \right], \quad (\text{A18})$$

where

$$\begin{aligned} \mathcal{D}_{\vec{k},\vec{k}'}^{4MS,1} = & \left\{ 2 \left[\mathcal{D}_{\vec{k}} (|u_{\vec{k}}|^2 |u_{\vec{k}'}|^2) + \mathcal{D}_{\vec{k}}^* (|v_{\vec{k}}|^2 |v_{\vec{k}'}|^2) \right] + \right. \\ & 2 \left[\mathcal{D}_{\vec{k}} (|u_{\vec{k}}|^2 |v_{\vec{k}'}|^2) + \mathcal{D}_{\vec{k}}^* (|v_{\vec{k}}|^2 |u_{\vec{k}'}|^2) \right] + \\ & 2 \left[\mathcal{D}_{\vec{k}} (u_{\vec{k}}^* v_{\vec{k}'}^* u_{\vec{k}} v_{\vec{k}}) + \mathcal{D}_{\vec{k}}^* (u_{\vec{k}} v_{\vec{k}'} u_{\vec{k}}^* v_{\vec{k}}^*) \right] \left. \right\} + \\ & \left\{ \left[\mathcal{D}_{\vec{k}} (|u_{\vec{k}}|^4) + \mathcal{D}_{\vec{k}}^* (|v_{\vec{k}}|^4) \right] + \right. \\ & 2 \left[\mathcal{D}_{\vec{k}} (|u_{\vec{k}}|^2 |v_{\vec{k}}|^2) + \mathcal{D}_{\vec{k}}^* (|u_{\vec{k}}|^2 |v_{\vec{k}}|^2) \right] \left. \right\} (\delta_{\vec{k}',\vec{k}} + 2\delta_{\vec{k}',-\vec{k}}) + \\ & \mathcal{D}_{\vec{k}}' [4u_0^* v_0^* u_{\vec{k}} v_{\vec{k}} + |u_0|^2 |u_{\vec{k}}|^2 + |v_0|^2 |v_{\vec{k}}|^2 + \\ & |u_0|^2 |v_{\vec{k}}|^2 + |v_0|^2 |u_{\vec{k}}|^2] \delta_{\vec{k}',0} + \\ & \mathcal{D}_{\vec{k}}' [|u_0|^2 |u_{\vec{k}}|^2 + |v_0|^2 |v_{\vec{k}}|^2 + |u_0|^2 |v_{\vec{k}}|^2 + |v_0|^2 |u_{\vec{k}}|^2] \delta_{\vec{k},0}, \end{aligned} \quad (\text{A19})$$

$$\begin{aligned} \mathcal{D}_{\vec{k},\vec{k}'}^{4MS,2} = & \left\{ 2 \left[\mathcal{D}_{\vec{k}} (u_{\vec{k}}^{*2} u_{\vec{k}}^2) + \mathcal{D}_{\vec{k}}^* (v_{\vec{k}}^{*2} v_{\vec{k}}^2) \right] + \right. \\ & 2 \left[\mathcal{D}_{\vec{k}} (u_{\vec{k}}^* v_{\vec{k}}^* u_{\vec{k}} v_{\vec{k}}) + \mathcal{D}_{\vec{k}}^* (v_{\vec{k}} u_{\vec{k}} v_{\vec{k}}^* u_{\vec{k}}^*) \right] \left. \right\} + \\ & \mathcal{D}_{\vec{k}}' [u_0^{*2} u_{\vec{k}}^2 + v_0^{*2} v_{\vec{k}}^2 + 2u_0^* v_0 u_{\vec{k}} v_{\vec{k}}^*] \delta_{\vec{k}',0} + \\ & \mathcal{D}_{\vec{k}}' [2u_0^* v_0 u_{\vec{k}} v_{\vec{k}}^*] \delta_{\vec{k},0}. \end{aligned} \quad (\text{A20})$$

The system Hamiltonian can be summarized as

$$H^{(T)} = H^{(c)} + H^{(d)} + H^{(mc)} + H^{(T,m)}, \quad (\text{A21})$$

where $H^{(c)} = \omega_c b^\dagger b$ is the cavity photon Hamiltonian, $H^{(d)} = i\bar{B}(b^\dagger - b) + \text{H.c.}$ is the external drive of the cavity field, $\bar{B} = \sqrt{\zeta_{c,ex} P_{in}}/(\hbar\omega_d)$, coupled to the cavity by $\zeta_{c,ex}$ via the input mirror, P_{in} is the input power, ω_d is the input drive frequency, $H^{(mc)} = -iD_0(b^\dagger c_0 - bc_0^\dagger)$, D_0 being the coupling constant of the cavity photon mode and the Kittel mode, and

$$H^{(T,m)} = H^{(3MS)} + H^{(4MS)} + \sum_{\vec{k}} \omega_{\vec{k}} c_{\vec{k}}^\dagger c_{\vec{k}}. \quad (\text{A22})$$

Appendix B: Fluctuations

We can write the field operators as $c_0 = \alpha_0 + \delta c_0$, $c_{\vec{k}} = \alpha_{\vec{k}} + \delta c_{\vec{k}}$ and $b = \beta + \delta b$, where $\{\delta c_0, \delta c_{\vec{k}}, \delta c_0^\dagger\}$ are the fluctuations around the steady state characterized by the complex numbers $\{\alpha_0, \alpha_{\vec{k}}, \beta\}$. We define the operators $\delta x_{0(\pm\vec{k})} = [\delta c_{0(\pm\vec{k})}^\dagger + \delta c_{0(\pm\vec{k})}]/2$, $\delta y_{0(\pm\vec{k})} = i[\delta c_{0(\pm\vec{k})}^\dagger - \delta c_{0(\pm\vec{k})}]/2$, $\delta X = [\delta b^\dagger + \delta b]/2$, $\delta Y = i[\delta b^\dagger - \delta b]/2$, $\mathbf{v} = (\delta x_0, \delta p_0, \delta x_{\vec{k}}, \delta p_{\vec{k}}, \delta x_{-\vec{k}}, \delta p_{-\vec{k}}, \delta X, \delta Y)^T$, which obey the linearized equation of motion (EOM)

$$\dot{\mathbf{v}} = \mathcal{O}\mathbf{v} + \mathbf{c}. \quad (\text{B1})$$

\mathbf{c} is the vector of the stochastic sources (discussed in more detail below)

$$\begin{aligned} \mathbf{c} = & \left[\sqrt{\zeta_{mm,0}} F_{mm,0}^{(x)}(t) + \sqrt{\zeta_{mp,0}} F_{mp,0}^{(x)}(t), \right. \\ & \sqrt{\zeta_{mm,0}} F_{mm,0}^{(p)}(t) + \sqrt{\zeta_{mp,0}} F_{mp,0}^{(p)}(t), \\ & \sqrt{\zeta_{mm,\vec{k}}} F_{mm,\vec{k}}^{(x)}(t) + \sqrt{\zeta_{mp,\vec{k}}} F_{mp,\vec{k}}^{(x)}(t), \\ & \sqrt{\zeta_{mm,\vec{k}}} F_{mm,\vec{k}}^{(p)}(t) + \sqrt{\zeta_{mp,\vec{k}}} F_{mp,\vec{k}}^{(p)}(t), \\ & \sqrt{\zeta_{mm,-\vec{k}}} F_{mm,-\vec{k}}^{(x)}(t) + \sqrt{\zeta_{mp,-\vec{k}}} F_{mp,-\vec{k}}^{(x)}(t), \\ & \sqrt{\zeta_{mm,-\vec{k}}} F_{mm,-\vec{k}}^{(p)}(t) + \sqrt{\zeta_{mp,-\vec{k}}} F_{mp,-\vec{k}}^{(p)}(t), \\ & \sqrt{\zeta_{c,0}} F_{c,0}^{(x)}(t) + \sqrt{\zeta_{c,ex}} F_{c,ex}^{(x)}(t), \\ & \left. \sqrt{\zeta_{c,0}} F_{c,0}^{(p)}(t) + \sqrt{\zeta_{c,ex}} F_{c,ex}^{(p)}(t) \right], \end{aligned} \quad (\text{B2})$$

where $F_{mm(mp),0(\pm\vec{k})}^{(x)}(t) = [F_{mm(mp),0(\pm\vec{k})}^\dagger(t) + F_{mm(mp),0(\pm\vec{k})}(t)]/2$, $F_{mm(mp),0(\pm\vec{k})}^{(p)}(t) = i[F_{mm(mp),0(\pm\vec{k})}^\dagger(t) - F_{mm(mp),0(\pm\vec{k})}(t)]/2$, $F_{c,0(ex)}^{(x)}(t) = [F_{c,0(ex)}^\dagger(t) + F_{c,0(ex)}(t)]/2$, and $F_{c,0(ex)}^{(p)}(t) = i[F_{c,0(ex)}^\dagger(t) - F_{c,0(ex)}(t)]/2$. \mathcal{O} is a square matrix that is governed by Heisenberg's equation for the Hamiltonian derived above and serves as well for the stability analysis. The symmetrized covariance matrix Λ consists of equal time correlations $\langle v_i v_j + v_j v_i \rangle / 2$, where $v_{i(j)}$ is i 'th (j 'th) element of \mathbf{v} , and contains the essential statistical parameters. Its EOM $\dot{\Lambda} = \mathcal{O}\Lambda + \Lambda\mathcal{O}^T + \Gamma$, where $\Gamma = \mathbf{c}\mathbf{c}^T$. Therefore, the steady state covariance matrix Λ_∞ is solution of the linear system of equation $\mathcal{O}\Lambda_\infty + \Lambda_\infty\mathcal{O}^T + \Gamma = 0$.

Rotating δX (δY) by an angle θ to a new variable $\delta X_\theta = (\delta b^\dagger e^{i\theta} + \delta b e^{-i\theta})/2$ [$\delta Y_\theta = i(\delta b^\dagger e^{i\theta} - \delta b e^{-i\theta})/2$] leads to a steady state covariance matrix $\Lambda_{\infty,\theta}$. We need the ellipticity of the total field fluctuation, i.e. the elements $[\Lambda_{\infty,\theta}]_{7(8),7(8)}$.

Let $(\alpha_0, \alpha_{\pm\vec{k}}, \beta)$ be the steady-state mean-field solutions of the EOMs (2)-(4). The matrix \mathcal{O} follows by linearizing these equations without noise terms around the steady state. For example, a term of the form $c_0^\dagger c_0 c_0$ is linearized as $2|\alpha_0|^2 \delta c_0 + \alpha_0^2 \delta c_0^\dagger$, where α_0 is the mean field solution. The covariance matrix can then be computed as explained above. The fluctuation ellipse of the total field is parameterized by

$$\xi_{sq} = \frac{\min \{[\Lambda_{\infty,\theta}]_{7(8),7(8)}\}}{\max \{[\Lambda_{\infty,\theta}]_{7(8),7(8)}\}}, \quad (\text{B3})$$

as well as θ_{sq} which is θ where $\{[\Lambda_{\infty,\theta}]_{7,7}\}$ is minimum.

1. 4MS effects

In the absence of microwaves, the “self-Kerr” term $K_1(c_0^\dagger c_0)^2$ of the Kittel mode, with

$K_1 = 2 \text{Re} [\mathcal{D}_{0,0}^{4MS,1} + \mathcal{D}_{0,0}^{4MS,2}]$, drives an initially coherent state through a cycle of periodic collapses and revivals in phase space, during which squeezed coherent states [64] and nonclassical superpositions of two or more coherent states in phase space develop [111]. The Kittel coherent state $|\alpha_0\rangle$ can be expanded in number states $|n\rangle$ as $|\alpha_0\rangle = \exp(-|\alpha_0|^2/2) \sum_n \alpha_0^n / \sqrt{n!} |n\rangle$. Ignoring dissipation, the temporal evolution of this state reads $|\Psi(t)\rangle = \exp(-K_1(c_0^\dagger c_0)^2 t) |\alpha_0\rangle = \exp(-|\alpha_0|^2/2) \sum_n (\alpha_0 \exp(-K_1 n t))^n / \sqrt{n!} |n\rangle$. $|\Psi(t)\rangle = |\alpha_0\rangle$ “revives” at $t = m\pi/K_1$, where $m \geq 0$ is integer. At $t = \pi/(mK_1)$ superposition “Schrödinger cat” states develop, for example $\Psi(\pi/(2K_1)) = 1/\sqrt{2}(\exp(-i\pi/4)|\alpha_0\rangle + \exp(i\pi/4)|-\alpha_0\rangle)$, where $|-\alpha_0\rangle$ is a Kittel coherent state with opposite phase. These processes cannot develop when the self-Kerr coefficient is small compared to the damping. However, the steady state in the presence of a constant coherent microwave drive remains coherent, but is “squeezed” by the non-linear terms as explained in the following.

The fluctuation ellipse of the Kittel mode is affected as well by its instability into a coherent superposition of the \vec{k} and $-\vec{k}$ modes via the interaction $c_{\vec{k}}^\dagger c_{-\vec{k}}^\dagger c_0 c_0$, leading to finite $\langle c_{\vec{k}}^\dagger c_{-\vec{k}}^\dagger \rangle$ and thereby $|\alpha_{\vec{k}}|^2 \left(e^{-i(\phi_{\vec{k}} + \phi_{-\vec{k}})} c_0 c_0 + e^{i(\phi_{\vec{k}} + \phi_{-\vec{k}})} c_0^\dagger c_0^\dagger \right)$, where $\phi_{\pm\vec{k}}$ is the phase of $\alpha_{\pm\vec{k}}$. With mean-field steady state of the Kittel mode α_0 , the effective Hamiltonian (after integrating out the cavity field) up to second order in δc_0 (δc_0^\dagger), and ignoring fluctuations $\delta c_{\pm\vec{k}}$ ($\delta c_{\pm\vec{k}}^\dagger$) in $\vec{k} \neq 0$, reads

$$H^{eff} = \Delta'_0 \delta c_0^\dagger \delta c_0 + \left[(K_s + \mathcal{G}) \delta c_0^\dagger \delta c_0^\dagger + H.c. \right] + \left[(\Delta'_0 + K_1 |\alpha_0|^2 \alpha_0 + \mathcal{G} \alpha_0^* + B'^*) \delta c_0^\dagger + H.c. \right], \quad (\text{B4})$$

where $\Delta'_0 = \{\Delta_0 - (D_0^2 \Delta)/(\Delta^2 + \zeta_c^2/4) + 4 \text{Re}[\mathcal{D}_{0,\vec{k}}^{4MS,1}] |\alpha_{\vec{k}}|^2\}$, $\mathcal{G} = \mathcal{D}_{0,\vec{k}}^{4MS,2} |\alpha_{\vec{k}}|^2 \exp[i(\phi_{\vec{k}} + \phi_{-\vec{k}})]$, $B' = (-i\Delta E D_0)/(\Delta^2 + \zeta_c^2/4)$, and $K_s = |\alpha_0|^2 e^{2i\phi_0}$, where ϕ_0 is the phase of α_0 . Since δc_0^\dagger and δc_0 in the last term vanish when operating on α_0 , to leading order

$$H^{eff} = \Delta'_0 \delta c_0^\dagger \delta c_0 + \left[(K_s + \mathcal{G}) \delta c_0^\dagger \delta c_0^\dagger + H.c. \right]. \quad (\text{B5})$$

We may diagonalize Eq. (B5) by the Bogoliubov transformation $\delta c_0' = u_0 \delta c_0 - v_0^* \delta c_0^\dagger$, which acts on the vacuum as a squeezing operator $\Pi(\epsilon) = \exp[1/2 \epsilon^* c_0^2 - 1/2 \epsilon c_0^{\dagger 2}]$, i.e. $\delta c_0' = \Pi(\epsilon) \delta c_0 \Pi^\dagger(\epsilon)$, where $\epsilon = -v_0 \tanh^{-1}(|v_0|/|u_0|)/|v_0|$. $\epsilon = r_s e^{2i\theta_s}$ parameterizes the fluctuation ellipse: e^{r_s} (e^{-r_s}) is the major (minor) diameter and θ_s is the angle of the major axis of the ellipse.

The squeezing parameters r_s and θ_s are functions of K_s and \mathcal{G} . When the Kittel mode is stable, $|\alpha_{\vec{k}}|^2 = \mathcal{G} = 0$.

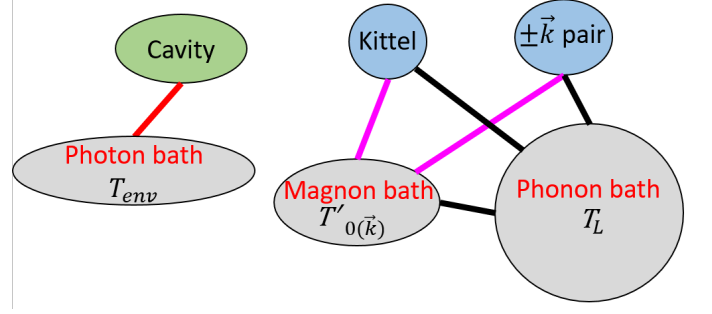


FIG. 10. Schematic of the total Hilbert space of photonic cavity mode, Kittel mode and selected pair of magnons with wave vector $\pm\vec{k}$, the baths, and the interactions. The driven magnetic modes relax by interaction with a bath of thermalized magnons at temperature $T'_{0(\pm\vec{k})}$ as depicted by purple lines as well as a (phonon) bath corresponding to Gilbert damping at temperature T_L (black lines). The bath of thermalized magnons also is in contact with the phonon bath. The cavity mode is in contact with a bath at temperature T_{env} , isolated from baths for magnon modes.

At the instability threshold of the Kittel mode, a pair of oppositely moving magnons with momenta \vec{k} and $-\vec{k}$ is excited and $|\alpha_{\vec{k}}|^2 \neq 0$. \mathcal{G} then may grow to become of the same order of magnitude as K_s , causing substantial changes in r_s and θ_s . It should be noted that the concept of squeezing was first introduced in spintronics in the context of squeezed magnon mediated spin transport [110].

2. Baths

The interaction of the driven state with thermalized magnons [47] and phonons [38, 112] govern the parts of stochastic force matrix Γ corresponding to the Kittel mode and the $\pm k \neq 0$ magnon pair. We disregard heating of the phonon bath which has a much larger specific heat than the magnon system. For a discussion on heat management of the phonon bath, see also Sec. VII. According to the fluctuation-dissipation theorem for thermal equilibrium and assuming temperatures to be high compared to the mode broadening, $\langle F_{mp,0(\pm\vec{k})}(t), F_{mp,0(\pm\vec{k})}^\dagger(t') \rangle = \zeta_{mp,0(\pm\vec{k})} (n_{th,0(\pm\vec{k})} + 1) \delta(t - t')$ and $\langle F_{mp,0(\pm\vec{k})}^\dagger(t), F_{mp,0(\pm\vec{k})}(t') \rangle = \zeta_{mp,0(\pm\vec{k})} n_{th,0(\pm\vec{k})} \delta(t - t')$, where $\zeta_{mp,0(\pm\vec{k})} \approx \alpha_G \omega_{0(\pm\vec{k})}$ is the phonon mediated dissipation of magnons, α_G the Gilbert damping constant, $n_{th,0(\pm\vec{k})}^{-1} = e^{\hbar\omega_{0(\pm\vec{k})}/(k_B T_L)} - 1$ the Planck distribution, T_L the phonon bath temperature, and k_B the Boltzmann constant [63]. The cavity field is assumed to be in contact with baths that keeps it at ambient temperature T_{env} . Therefore, $\langle F_{c,0(ex)}(t), F_{c,0(ex)}^\dagger(t') \rangle = \zeta_{c,0(ex)} (n_{th,\text{env}} + 1) \delta(t - t')$ and $\langle F_{c,0(ex)}^\dagger(t), F_{c,0(ex)}(t') \rangle = \zeta_{c,0(ex)} n_{th,\text{env}} \delta(t - t')$

$[\zeta_{c,0(e\bar{x})}]$ is the decay rate of the cavity field by scattering to internal cavity modes (external leakage), and $n_{th,env}^{-1} = e^{\hbar\omega_c/k_B T_{env}} - 1$. The noise sources $F_{mm,0}(t)$ and $F_{mm,\pm\vec{k}}(t)$ are generated by thermal magnon bath at temperatures discussed in the following.

The 4MS driven modes with momenta $0(\pm\vec{k})$ around frequency ω_0 can relax to other magnon modes by magnon-magnon scatterings. We can estimate the temperature of the associated thermal cloud $T'_{0(\pm\vec{k})}$ by considering the transition probability \mathcal{P}_p [46, 113]

$$\mathcal{P}_p = \frac{2\pi}{\hbar} \int |\langle \Phi' | H_t | \Phi \rangle|^2 \varrho(E) \delta(E' - E) dE, \quad (B6)$$

where the initial state $|\Phi\rangle = \prod_{\vec{k}'} |n_{\vec{k}'}\rangle$ ($\vec{k}' = \{0, \pm\vec{k}\}$) and the final state $|\Phi'\rangle = \prod_{\vec{k}''} |n_{\vec{k}''}\rangle$ (\vec{k}'' corresponds to thermal magnon bath modes) are expressed in the magnon number basis with the density of states $\varrho(E)$. The cross-Kerr term matrix elements in the transition Hamiltonian H_t vanish and elastic three-magnon processes are weak under the condition $H_{ext} \gg M_s/3$ (the assumption in our work), which leads to $H_t = \sum_{\vec{k}'', \vec{k}'} \mathcal{D}_{\vec{k}'', \vec{k}'}^{4MS,2} c_{-\vec{k}'', \vec{k}'}^\dagger c_{-\vec{k}', 0}^\dagger c_{-\vec{k}', \vec{k}'} + \text{H.c.}$. The scattering rate of driven magnons into \vec{k}'' magnon modes

$$\begin{aligned} \mathcal{T}_{sc} = & \sum_{\vec{k}''} \sum_{\vec{k}'} 2\hbar\omega_{\vec{k}'} \left[\mathcal{P}_p \left(n_{\vec{k}'} \rightarrow n_{\vec{k}'} + \delta_{\vec{k}', \pm\vec{k}} + 2\delta_{\vec{k}', 0} \right) \right. \\ & \left. - \mathcal{P}_p \left(n_{\vec{k}'} \rightarrow n_{\vec{k}'} - \delta_{\vec{k}', \pm\vec{k}} - 2\delta_{\vec{k}', 0} \right) \right] \\ = & \sum_{\vec{k}''} \sum_{\vec{k}'} 4\pi\omega_{\vec{k}'} \varrho(\hbar\omega_{\vec{k}''}) \left| \hbar \mathcal{D}_{\vec{k}'', \vec{k}'}^{4MS,2} \right|^2 \left[n_{\vec{k}'}^2 (2n_{\vec{k}'', 0} + 1) + \right. \\ & n_{\vec{k}'} n_{\vec{k}''} (6\delta_{\vec{k}', 0} + 4\delta_{\vec{k}', \pm\vec{k}}) + n_{\vec{k}''} (4\delta_{\vec{k}', 0} + 2\delta_{\vec{k}', \pm\vec{k}}) + \\ & \left. n_{\vec{k}'} (3\delta_{\vec{k}', 0} + 2\delta_{\vec{k}', \pm\vec{k}}) + n_{\vec{k}'', 0}^2 (2n_{\vec{k}'} + 1) \times (2\delta_{\vec{k}', 0} + \delta_{\vec{k}', \pm\vec{k}}) \right], \end{aligned} \quad (B7)$$

where $\mathcal{P}_p \left(n_{\vec{k}'} \rightarrow n_{\vec{k}'} \pm \delta_{\vec{k}', \pm\vec{k}} \pm 2\delta_{\vec{k}', 0} \right)$ corresponds to a transition described by Eq. (B6) that changes magnon number in \vec{k}' sector by two. In the steady state, the scattered magnon flux into the \vec{k}'' modes equals their dissipation rate to the lattice

$$\mathcal{T}_d = \sum_{\vec{k}''} \hbar\omega_{\vec{k}''} \zeta_{mp, \vec{k}''} \left(n_{\vec{k}''} - n_{th, \vec{k}''} \right), \quad (B8)$$

where $n_{th, \vec{k}''}$ is the thermal equilibrium determined by the phonon bath temperature T_L . In order to estimate $n_{\vec{k}''}$ of the magnon bath after heating by the driven magnons, we assume \vec{k}'' close to \vec{k} that dominate $|\mathcal{D}_{\vec{k}'', 0}^{4MS,2}|$, and assume $\omega_{\vec{k}''} = \omega_0 = \omega_{\pm\vec{k}}$. These assumptions also lead to $T_{\vec{k}''} = T_0$, i.e. $n_{th, \vec{k}''} = n_{th, 0}$, $\zeta_{mp, \vec{k}''} = \zeta_{mp, 0}$, and $\varrho(\hbar\omega_{\vec{k}''}) = 2/(\pi\hbar\zeta_{mp, 0})$. For a

YIG sphere with 0.1 mm radius $|\mathcal{D}_{\vec{k}'', 0}^{4MS,2}| \sim 10^{-8}$, and for $\bar{B} = 3.3 \times 10^{13}$ that we use mainly for the results of this work, the largest steady states after instabilities $n_0 \sim n_{\pm\vec{k}} \sim 10^{13}$ [see e.g. Fig. 1(c) and Fig. 2]. Therefore, we can estimate the maximal heating of the magnon cloud bath in our calculations by equating the integrands in Eq. (B7) and Eq. (B8). A phonon bath of $T_L = 1$ K, $\omega_{\vec{k}''} = \omega_0 = 10^{11}/(2\pi) 1/\text{s}$, i.e. $n_{th, \vec{k}''} = 0.87$, $\zeta_{mp, 0} = 1$ MHz, determines the mean \vec{k}'' magnon number to be $n_{\vec{k}''} = 1.13$ or a temperature $T'_{0(\pm\vec{k})} \sim 1.2$ K, i.e. the magnon modes of the thermal cloud are heated by 0.2 degrees. The correlators of magnon thermal cloud noise source $\langle F_{mm, 0(\pm\vec{k})}(t), F_{mm, 0(\pm\vec{k})}^\dagger(t') \rangle = \zeta_{mm, 0(\pm\vec{k})} (n'_{th, 0(\pm\vec{k})} + 1) \delta(t - t')$ and $\langle F_{mm, 0(\pm\vec{k})}^\dagger(t), F_{mm, 0(\pm\vec{k})}(t') \rangle = \zeta_{mm, 0(\pm\vec{k})} n'_{th, 0(\pm\vec{k})} \delta(t - t')$, where $1/n'_{0(\pm\vec{k})} = e^{\hbar\omega_{0(\pm\vec{k})}/k_B T'_{0(\pm\vec{k})}} - 1$, and in YIG $\zeta_{mm, 0(\pm\vec{k})} \sim 1$ MHz [47, 114].

Schematically, the driven modes and the baths are linked as in Fig. 10. As temperature goes towards zero, the reservoir correlation time ($\hbar/k_B T$) reaches infinity, and the Markovian bath approximation breaks down and the noise correlation functions can not be assumed as delta function anymore (i.e. the noise becomes colored) [63]. Moreover, the dominant magnon dissipation source at temperatures < 1 K is not the phonon bath anymore [2]. Therefore, the present approximations hold for temperatures $T_{env} \geq 1$ K. In our calculations, we need to set only T_{env} , which determines $T_L \approx T_{env}$, and consequently $T'_{0(\pm\vec{k})}$ which is governed by the rate equations discussed earlier. It should again be pointed out that realistically, as discussed in Sec. VII, $T_L \neq T_{env}$, but with proper heat management the difference can be kept small.

Appendix C: Scaling and master equation

The observable consequences of non-classical behavior such as entanglement can be most reliably assessed by the density matrix calculated from the first principles of quantum mechanics, which is possible by limiting the Hilbert space of the total Hamiltonian $H^{(T)}$. This can be done by scaling down the drive amplitude \bar{B} with a coefficient Q as \bar{B}/Q , while scaling up the fourth order terms by Q^2 , in order to preserve the nonlinearities. This scaling compresses, but preserves the details of the phase space, such as the number of fixed points and their relative positions. The costs of the scaling are loss of transient states that in the physical system might appear as steady states. For example, in the scaled system, we never find the limit cycle solution for the Kittel mode predicted by the (semi-)classical method, see Fig. 2, because the effects of quantum fluctuations are enhanced by the reduced distance between the attractors in phase space. Actually, quantum fluctu-

ations always destroy the classical bistability in the self-Kerr Hamiltonian, but on very long time scales when energy minima are well separated [60]. In the off-resonant regime $|\omega_d - \omega_c| \gg D_0$, we may adiabatically remove (integrate out) the cavity field, which reduces Hilbert space to the Kittel mode and connected $\pm \vec{k}$ magnon pair $n_{F,0} \times n_{F,\vec{k}}^2$, where $n_{F,0}$ ($n_{F,\vec{k}}$) is the number of Fock (number) states into which we expand the steady state density matrix [63, 64]. As an example of how the scaling preserves the nonlinearity effects, one can note that the bistable points for the Kittel mode in the absence of 4MS are at $n_0^\pm = [-2\Delta'_0 \pm (\Delta'_0{}^2 - 3\zeta_{m,0}^2)^{1/2}]/(6K_1)$ [60], where n_0^\pm is the mean number of Kittel mode magnons in the two bistable points, Δ'_0 is the effective detuning of the Kittel mode from the drive frequency, and $K_1 = 2\text{Re}[\mathcal{D}_{0,0}^{4MS,1} + \mathcal{D}_{0,0}^{4MS,2}]$. This number is too large for an exact computation, but we may scale n_0^\pm down by a factor $1/Q^2$. We keep dissipation constant during scaling. This is the scaling that we use in our analysis. One could alternatively scale the dissipation by $1/Q$, for which the detunings at which bistability emerges scale like $1/Q$, while the 4MS coefficients should be scaled by Q rather than Q^2 .

We chose Q which allows us to shrink the Hilbert space to $n_{F,0} = 15$ and $n_{F,\pm\vec{k}} = 7$, which is small enough to numerically solve the master equation for the density matrix $\hat{\rho}$:

$$\begin{aligned} \dot{\hat{\rho}} = & -i[H'^{(T)}, \hat{\rho}] + \\ & \sum_{\vec{k}' \in \{0, \vec{k}, -\vec{k}\}} [\zeta_{mp, \vec{k}'} n_{th, \vec{k}'} + \zeta_{mm, \vec{k}'} n'_{th, \vec{k}'}] L_{\vec{k}'}(\hat{\rho}) + \\ & \sum_{\vec{k}' \in \{0, \vec{k}, -\vec{k}\}} \left[\frac{\zeta_{mp, \vec{k}'}}{2} + \frac{\zeta_{mm, \vec{k}'}}{2} \right] L'_{\vec{k}'}(\hat{\rho}), \end{aligned} \quad (\text{C1})$$

where $L_{\vec{k}'}$ and $L'_{\vec{k}'}$ are the Lindblad operators governing the dissipation in the Born-Markov approximation [63]

$$L_{\vec{k}'} = c_{\vec{k}'} \hat{\rho} c_{\vec{k}'}^\dagger + c_{\vec{k}'}^\dagger \hat{\rho} c_{\vec{k}'} - \hat{\rho} c_{\vec{k}'} c_{\vec{k}'}^\dagger, \quad (\text{C2})$$

$$L'_{\vec{k}'} = 2c_{\vec{k}'} \hat{\rho} c_{\vec{k}'}^\dagger - c_{\vec{k}'}^\dagger c_{\vec{k}'} \hat{\rho} - \hat{\rho} c_{\vec{k}'}^\dagger c_{\vec{k}'}. \quad (\text{C3})$$

Eq. (C1) can be written in terms of a superoperator matrix \mathcal{L} as $\dot{\hat{\rho}} = \mathcal{L}\hat{\rho}$. The steady state of the density matrix, ρ_{ss} , satisfies $\hat{\rho}_{ss} = \mathcal{L}\hat{\rho}_{ss} = 0$. Therefore, we search for the eigenvector with zero eigenvalue of the superoperator matrix \mathcal{L} . This can be done in two ways. First method: as the steady state equation $\mathcal{L}\hat{\rho} = 0$ suggests, the process begins by reforming the matrix ρ into a vector and reforming \mathcal{L} to conserve the equation. Then what remains is simply getting the eigenvector corresponding to the smallest eigenvalue which is zero by construction. This can be done using Lanczos loops. Second method: the matrix \mathcal{M} which gives $\mathcal{M}\rho = [\text{Tr}(\rho) = 1, 0, 0, \dots]^T$, is simply known. Using this matrix and $\mathcal{L}\rho = 0$, we have $(\mathcal{L} + \mathcal{M})\rho = \mathcal{M}\rho = [1, 0, 0, \dots]^T$. Now ρ_{ss} is reached by simply solving this linear system of equations. We use

the second method which is much faster, more scalable and more accurate. We also use methods pertaining to sparse matrices in order to speed up and maximize the computationally tractable Hilbert space.

Appendix D: Entanglement measures

1. Logarithmic negativity

A bipartite system (“Alice and Bob”) is separable when $\hat{\rho} = \sum_i \eta_i \hat{\rho}_{i,1} \otimes \hat{\rho}_{i,2}$, where η_i is a coefficient, $\hat{\rho}$ is the total density operator of the mixed state of system 1 and 2, $\hat{\rho}_{i,1(2)}$ is the density operator of system 1 (2) for the pure state i , and \otimes denotes the direct product. Here, for introduction, we focus on a pure state $\hat{\rho} = \hat{\rho}_1 \otimes \hat{\rho}_2$, since the treatment can be easily extended to mixed states. Since $(\hat{\rho}_1)^T = \hat{\rho}_1^*$ is a well behaved density matrix with positive eigenvalues, a negative eigenvalue of $\hat{\rho}' = (\hat{\rho}_1)^T \otimes \hat{\rho}_2$ implies that the state would not be separable into its parts 1 and 2; in other words the state would be entangled. This negative partial transpose (NPT) criterium is generally a sufficient condition for entanglement [67, 73, 74]. Vidal and Werner [75] introduced an entanglement measure based on NPT that quantifies the degree with which $\hat{\rho}'$ fails to be positive. The trace norm $\|\rho'\|_1 = \text{tr} \sqrt{\rho'^\dagger \rho'} = 1 + 2|\sum_i \mu_i| = 1 + 2\mathbf{n}(\rho)$, where the sum is over all negative eigenvalues $\mu_i < 0$ of the partially transposed density matrix, and $\mathbf{n}(\rho)$ is referred to as *negativity*. The *logarithmic negativity* $E_{LN} = \log_2 \|\rho'\|_1 \geq E_D$ bounds E_D , the rate at which entanglement can be distilled using local operations and classical communications, the so-called LOCC [67, 70–72]. For example, $E_D = 0.4$ means that 10 copies of the state can in principle produce 4 perfect Einstein-Podolsky-Rosen (EPR) states [68]. EPR states are non-local entangled states shared between two distinct particles (modes). Examples are spin singlet states and two-mode squeezed states.

When evaluating e.g. bipartite entanglement, a system of modes should be divided in several parts, each part consisting of one or more modes. It should be noted that the photon mode forms a hybridized mode (polariton) with the Kittel mode, and this polariton should be considered as one mode. Therefore, here we are dealing with essentially a maximally tripartite system, the Kittel mode-photon polariton and the two modes of the instability driven $\pm \vec{k}$ pair. In this case, one should evaluate entanglement between each part ρ_{0p} (‘0p’ in the subscript indicates the part corresponding to Kittel-photon polariton), $\rho_{-\vec{k}}$, and $\rho_{\vec{k}}$ with the other two parts joined as one part, $\rho_{\vec{k}, -\vec{k}} = \hat{\rho}_{\vec{k}} \otimes \hat{\rho}_{-\vec{k}}$, $\rho_{0p, \vec{k}}$, and $\rho_{0p, -\vec{k}}$. Therefore, there are only two distinct configurations as shown in Fig. 6, with corresponding logarithmic negativities $E_{LN, \pm \vec{k} \{0p, \mp \vec{k}\}}$ and $E_{LN, 0p \{\pm \vec{k}\}}$. From here on and in the main text, we drop ‘p’ in ‘0p’ for simplicity.

The covariance matrix Λ in Appendix B can be

used to calculate $E_{LN,\pm\vec{k}\{0p,\mp\vec{k}\}}$ and $E_{LN,0p\{\pm\vec{k}\}}$ [75]. For E_{LN} calculated from covariance matrices, we add a superscript ‘L’, i.e. E_{LN}^L . Transposition corresponds to time reversal, i.e. reversing the sign of momentum. The partially transposed covariance matrix Λ' is obtained from Λ by negating the elements connecting momentum of the mode (modes) of one part to the positions of the same part as well as to positions and momenta of the modes of the other parts. For example, for evaluation of $E_{LN,\pm\vec{k}\{0p,\mp\vec{k}\}}^L$, $[\Lambda']_{1(3,4,5,6,7,1,3,4,5,6,7),2(2,2,2,2,2,8,8,8,8,8)} = -[\Lambda]_{1(3,4,5,6,7,1,3,4,5,6,7),2(2,2,2,2,2,8,8,8,8,8)}$, where $[\Lambda^{(o)}]_{1(3,4,\dots),2(2,2,\dots)}$ indicates $[\Lambda^{(o)}]_{1,2}$, $[\Lambda^{(o)}]_{3,2}$, $[\Lambda^{(o)}]_{4,2}$, \dots , respectively, and $\Lambda'^T = \Lambda'$. The logarithmic negativities for Gaussian distributed states [75] are

$$E_{LN,i}^L = \sum_{i=1}^8 \mathcal{Y}(\mathfrak{d}_i), \quad (\text{D1})$$

where i is either $\pm\vec{k}\{0,\mp\vec{k}\}$ or $0\{\pm\vec{k}\}$, $\mathcal{Y}(\mathfrak{d}_i) = -\log_2(2\mathfrak{d}_i)$ if $2\mathfrak{d}_i < 1$ and zero otherwise, \mathfrak{d}_i is an eigenvalue of $\sigma^{-1}\Lambda'$, and σ is a 8×8 block-diagonal matrix with blocks formed by the Pauli matrix σ_x . This evaluation fails for states that are far from being Gaussian.

We also evaluate E_{LN} from the density matrix of the steady states ρ_{ss} achieved from solving the quantum master equation corresponding to the scaled system as described in Appendix C. This is a straightforward calculation, as one only requires to transpose the ρ_{ss} components corresponding to the Hilbert space of one of the parts for each bipartite configuration. For E_{LN} calculated from density matrices, we add a superscript ‘q’, i.e. E_{LN}^q . ρ_{ss} is a matrix with entries corresponding to $|i,j,k\rangle\langle i',j',k'|$, i (i'), j (j'), and k (k') refer to the i ’th (i' ’th), j ’th (j' ’th), and k ’th (k' ’th) Fock (number, level) state of the Kittel mode, \vec{k} mode, and $-\vec{k}$ mode, respectively. Now, for obtaining e.g. $E_{LN,0\{\pm\vec{k}\}}^q$, we form partial transposed density matrix ρ_{ss}^{PT} with entries $|i',j,k\rangle\langle i,j',k'|$ equivalent to entries $|i,j,k\rangle\langle i',j',k'|$ of ρ_{ss} . Now diagonalize ρ_{ss}^{PT} , and obtain its negative eigenvalues which lead directly to $E_{LN,0\{\pm\vec{k}\}}^q$. Similar partial transposition leads to $E_{LN,\pm\vec{k}\{0,\mp\vec{k}\}}^q$.

2. Entanglement of formation

The logarithmic negativity gives an upper bound for distillable entanglement E_D of a bipartite state. Even if $E_D = 0$ for a general mixed state, it does not mean that there is no entanglement in that state. This concept manifests itself in the reverse process, i.e. the required number of completely entangled particles for building a certain bipartite state, which has a different measure named entanglement of formation, E_F [79, 80]. This quantity is the same as E_D for pure states [70]. In this case, both are equivalent to the von Neumann entropy

$E_{vN} = \text{Tr}\rho_{1(2)} \log_2 \rho_{1(2)}$ where $\rho_{1(2)} = \text{Tr}_{2(1)}\rho$ (tracing over the part 2 (1) of the bipartite state), and ρ is the total density matrix of the bipartite system and $\rho_{1(2)}$ is the density matrix of part 1 (2). However, when we deal with mixed states, there is no closed formula for E_F . For a bipartite mixed state, E_F is the minimum E_{vN} among different realizations of a mixed state using pure states $\rho = \sum_i p_i |\Upsilon_i\rangle\langle\Upsilon_i|$, where Υ_i is a pure state. There are infinite ways of assigning an ensemble of $\{p_i, \Upsilon_i\}$ for a mixed state. Even though there are analytical expressions for mixed state of two qubits [80] as well as approximate closed form solution and bounds for two-mode Gaussian states [82], evaluating E_F for a general system can only be done using numerical methods. We utilize the algorithm given in Ref. [81] for finding E_F . Here, we give a summary of the algorithm we used:

- (1) Perform a singular value decomposition on the mixed state $\rho = U_\rho \times S_\rho \times V_\rho$, where S_ρ is a diagonal matrix containing all the singular values in descending order. As the numerical method in Ref. [81] becomes less effective at large dimensions of ρ , we should perform a cutoff much similar to the one performed in density matrix renormalization group calculation method [115]. We keep N_{co} largest values of S_ρ and discard the rest, and also discard the corresponding columns of U_ρ and corresponding rows of V_ρ , to reach S'_ρ , U'_ρ and V'_ρ , respectively. Therefore, we have reached a decomposition of the mixed state ρ by pure states in a space of smaller dimension, $\rho = \sum_i^{N_{co}} p_i |\Upsilon_i\rangle\langle\Upsilon_i|$, where p_i are entries of S'_ρ and $|\Upsilon_i\rangle$ are rows of V'_ρ .
- (2) Form a random unitary matrix \mathcal{U} of dimension $N_{co} \times N_{co}$, with the method detailed in Ref. [116]. Subsequently, form the density matrix $\rho' = \sum_i^{N_{co}} |\Upsilon'_i\rangle\langle\Upsilon'_i|$, where $|\Upsilon'_i\rangle = \sum_j^{N_{co}} \mathcal{U}_{ji} |\Upsilon_j\rangle$.
- (3) Evaluate E_{vN} for ρ' , and memorize its value as $E_{vN,0}$.
- (4) Form a random hermitian matrix \mathcal{R} with each of the matrix entries of row (column) i (j) having Gaussian distribution with variance $(1 \pm \delta_{ij})/N_{co}$ for real and imaginary parts, respectively.
- (5) Form the unitary matrix $\mathcal{U}' = \mathcal{U} \exp[i\chi\mathcal{R}]$. If it is the first time for this step, set $\chi = \chi_0$, if not, scale down χ by $\Xi < 1$.
- (6) Form ρ' corresponding to \mathcal{U}' similar to what was described in step (2). Evaluate the corresponding E_{vN} , and memorize its value as $E_{vN,1}$.
- (7) If $E_{vN,1} < E_{vN,0}$, accept the move, i.e. set $E_{vN,0} = E_{vN,1}$ and $\mathcal{U} = \mathcal{U}'$.
- (8) Repeat steps (5)-(7), N_χ times. Memorize all the accepted values of $E_{vN,1}$.
- (9) Repeat steps (4)-(8), $N_\mathcal{R}$ times.
- (10) Repeat steps (2)-(9), $N_\mathcal{U}$ times.
- (11) The minimum among all the memorized values of $E_{vN,1}$ is the entanglement of formation E_F .

We only calculate $E_{F,0\{\pm\vec{k}\}}$, and for that we set $N_{co} = 8$, $N_\chi = 20$, $N_\mathcal{R} = 20$, $N_\mathcal{U} = 500$, $\chi_0 = 0.3$, $\Xi = 2/3$. In Fig. 11, we show E_{vN} for accepted moves, i.e. memorized $E_{vN,1}$, in the case of injection locking pumping

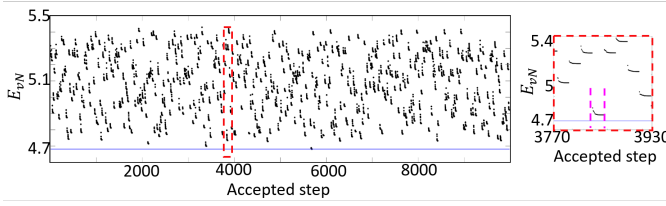


FIG. 11. The von Neumann entropy of each accepted step ($E_{vN,1}$) in the process for calculation of entanglement of formation E_F . The right panel is a zoom in of the area within the red-dashed rectangle in the left panel. The points in between the purple dashed lines belong to minimizing process for a certain initial random unitary matrix.

amplitude $B_l = 10^{12}$ (see Fig. 8). The large spread of E_{vN} for possible decompositions of the mixed state into pure states shows how delicate finding E_F for a general mixed state is. In the right panel of Fig. 11, a zoomed in section of the left panel is shown, and the data points surrounded by purple dashed-lines correspond to memorized $E_{vN,1}$ values in $N_{\mathcal{R}}$ iterations of steps (4)-(8) for a certain initial random unitary matrix generated in step (2). The blue line in Fig. 11 indicates the minimum among all values of accepted $E_{vN,1}$, i.e. the entanglement of formation E_F .

-
- [1] X. Zhang, C.-L. Zou, L. Jiang, and H. X. Tang, Phys. Rev. Lett. **113**, 156401 (2014).
 - [2] Y. Tabuchi, S. Ishino, T. Ishikawa, R. Yamazaki, K. Usami, and Y. Nakamura, Phys. Rev. Lett. **113**, 083603 (2014).
 - [3] A. Osada, R. Hisatomi, A. Noguchi, Y. Tabuchi, R. Yamazaki, K. Usami, M. Sadgrove, R. Yalla, M. Nomura, and Y. Nakamura, Phys. Rev. Lett. **116**, 223601 (2016).
 - [4] X. Zhang, N. Zhu, C.-L. Zou, and H. X. Tang, Phys. Rev. Lett. **117**, 123605 (2016).
 - [5] J. A. Haigh, A. Nunnenkamp, A. J. Ramsay, and A. J. Ferguson, Phys. Rev. Lett. **117**, 133602 (2016).
 - [6] S. Sharma, Y. M. Blanter, and G. E. W. Bauer, Phys. Rev. B **96**, 094412 (2017).
 - [7] H. Huebl, C. W. Zollitsch, J. Lotze, F. Hocke, M. Greifenstein, A. Marx, R. Gross, and S. T. B. Goennenwein, Phys. Rev. Lett. **111**, 127003 (2013).
 - [8] J. M. Raimond, M. Brune, and S. Haroche, Rev. Mod. Phys. **73**, 2001 (2001).
 - [9] H. Mabuchi and A. C. Doherty, Science **298**, 1372 (2002).
 - [10] Z.-L. Xiang, S. Ashhab, J. Q. You, and F. Nori, Rev. Mod. Phys. **85**, 623 (2013).
 - [11] Y. Tabuchi, S. Ishino, A. Noguchi, T. Ishikawa, R. Yamazaki, K. Usami, and Y. Nakamura, Science **349**, 405 (2015).
 - [12] J. A. Haigh, S. Langenfeld, N. J. Lambert, J. J. Baumberg, A. J. Ramsay, A. Nunnenkamp, and A. J. Ferguson, Phys. Rev. A **92**, 063845 (2015).
 - [13] X. Zhang, C.-L. Zou, N. Zhu, F. Marquardt, L. Jiang, and H. X. Tang, Nat. Commun. **6**, 8914 (2015).
 - [14] L. Bai, M. Harder, Y. P. Chen, X. Fan, J. Q. Xiao, and C.-M. Hu, Phys. Rev. Lett. **114**, 227201 (2015).
 - [15] G. Bertotti, I. D. Mayergoyz, and C. Serpico, *Nonlinear magnetization dynamics in nanosystems*, Elsevier (2009).
 - [16] D. D. Stancil and A. Prabhakar, *Spin waves*, Springer (2009).
 - [17] V. E. Demidov, O. Dzyapko, S. O. Demokritov, G. A. Melkov, and A. N. Slavin, Phys. Rev. Lett. **99**, 037205 (2007).
 - [18] V. E. Demidov, O. Dzyapko, S. O. Demokritov, G. A. Melkov, and A. N. Slavin, Phys. Rev. Lett. **100**, 047205 (2008).
 - [19] A. A. Serga, V. S. Tiberkevich, C. W. Sandweg, V. I. Vasyuchka, D. A. Bozhko, A. V. Chumak, T. Neumann, B. Obry, G. A. Melkov, A. N. Slavin, and B. Hillebrands, Nat. Commun. **5**, 3452 (2013).
 - [20] D. A. Bozhko, A. A. Serga, P. Clausen, V. I. Vasyuchka, F. Heussner, G. A. Melkov, A. Pomyalov, V. S. Lvov, and B. Hillebrands, Nat. Phys. **12**, 1057 (2016).
 - [21] S. A. Bender, R. A. Duine, and Y. Tserkovnyak, Phys. Rev. Lett. **108**, 246601 (2012).
 - [22] P. H. Bryant, C. D. Jeffries, and K. Nakamura, Phys. Rev. A **38**, 4223 (1988).
 - [23] S. M. Rezende and F. M. D. Aguiar, Proc. IEEE **78**, 893 (1990).
 - [24] A. Slavin and V. Tiberkevich, IEEE Trans. Magn. **45**, 1875 (2009).
 - [25] V. E. Demidov, S. Urazhdin, H. Ulrichs, V. Tiberkevich, A. Slavin, D. Baither, G. Schmitz, and S. O. Demokritov, Nature Mater. **11**, 1028 (2012).
 - [26] S. Kaka, M. R. Pufall, W. H. Rippard, T. J. Silva, S. E. Russek, and J. A. Katine, Nature **437**, 389 (2005).
 - [27] M. Elyasi, C. S. Bhatia, and H. Yang, J. Appl. Phys. **117**, 063907 (2015).
 - [28] A. N. Slavin and I. V. Rojdestvenski, IEEE Trans. Magn. **30**, 37 (1994).
 - [29] O. Buttner, M. Bauer, S. O. Demokritov, B. Hillebrands, Y. S. Kivshar, V. Grimalsky, Y. Rapoport, T. Shevchenko, M. P. Kostylev, B. A. Kalinikos, and A. N. Slavin, J. Appl. Phys. **87**, 5088 (2000).
 - [30] M. Wu, B. A. Kalinikos, L. D. Carr, and C. E. Patton, Phys. Rev. Lett. **96**, 187202 (2006).
 - [31] M. Elyasi, K. Sato, and G. E. W. Bauer, Phys. Rev. B **99**, 134402 (2019).
 - [32] A. V. Chumak, A. A. Serga, and B. Hillebrands, Nat. Commun. **5**, 4700 (2014).
 - [33] Y.-P. Wang, G.-Q. Zhang, D. Zhang, X.-Q. Luo, W. Xiong, S.-P. Wang, T.-F. Li, C.-M. Hu, and J. Q. You, Phys. Rev. B **94**, 224410 (2016).
 - [34] Y.-P. Wang, G.-Q. Zhang, D. Zhang, T.-F. Li, C.-M. Hu, and J. Q. You, Phys. Rev. Lett. **120**, 057202 (2018).
 - [35] H. G. Craighead, Science **290**, 1532 (2000).
 - [36] J. S. Aldridge and A. N. Cleland, Phys. Rev. Lett. **94**, 156403 (2005).
 - [37] O. Shevchuk, V. Singh, G. A. Steele, and Y. M. Blanter, Phys. Rev. B **92**, 195415 (2015).

- [38] A. Ruckriegel and P. Kopietz, Phys. Rev. Lett. **115**, 157203 (2015).
- [39] D. Lachance-Quirion, Y. Tabuchi, S. Ishino, A. Noguchi, T. Ishikawa, R. Yamazaki and Y. Nakamura, Sci. Adv. **3**, 1603150 (2017).
- [40] M. Aspelmeyer, T. J. Kippenberg, and F. Marquardt, Rev. Mod. Phys. **86**, 1391 (2014).
- [41] F. Marquardt, J. G. E. Harris, and S. M. Girvin, Phys. Rev. Lett. **96**, 103901 (2006).
- [42] J. Qian, A. A. Clerk, K. Hammerer, and F. Marquardt, Phys. Rev. Lett. **109**, 253601 (2012).
- [43] A. Nunnenkamp, K. Børkje, J. G. E. Harris, and S. M. Girvin, Phys. Rev. A **82**, 021806 (2010).
- [44] S. Rips, M. Kiffner, I. Wilson-Rae, and M. J. Hartmann, New J. Phys. **14**, 023042 (2012).
- [45] G. Wang, L. Huang, Y.-C. Lai, and C. Grebogi, Phys. Rev. Lett. **112**, 110406 (2014).
- [46] R. M. White, *Quantum theory of magnetism*, Springer (2006).
- [47] S. M. Rezende, Phys. Rev. B **79**, 174411 (2009).
- [48] L. R. Walker, Phys. Rev. **105**, 390 (1957).
- [49] L. R. Walker, J. Appl. Phys. **29**, 318 (1958).
- [50] R. W. Damon and J. R. Eshbach, J. Phys. Chem. Solids **19**, 308 (1961).
- [51] B. A. Kalinikos and A. N. Slavin, J. Phys. C: Solid State Phys. **19**, 7013 (1986).
- [52] M. J. Hurben and C. E. Patton, J. Magn. Magn. Mater. **139**, 263 (1995).
- [53] H. Suhl, Phys. Chem. Solids **1**, 209 (1957).
- [54] R. G. E. Morris, A. F. van Loo, and S. Kosen, Sci. Rep. **7**, 11511 (2017).
- [55] N. Zhu, H. Chang, A. Franson, T. Liu, X. Zhang, E. J.-Halperin, Mingzhong Wu, and Hong X. Tang, Appl. Phys. Lett. **110**, 252401 (2017).
- [56] F. Heyroth, C. Hauser, P. Trempler, P. Geyer, F. Syrowatka, R. Dreyer, S. G. Ebbinghaus, G. Woltersdorf, and G. Schmidt, arXiv:1802.03176v2 (2019).
- [57] P. Hansen, J. Appl. Phys. **45**, 3638 (1974).
- [58] H. Chang, P. Li, W. Zhang, T. Liu, A. Hoffmann, L. Deng, and M. Wu, IEEE Magn. Lett. **5**, 6700104 (2014).
- [59] G. Gibson and C. Jeffries, Phys. Rev. A **29**, 811 (1984).
- [60] V. V. Naletov, G. de Loubens, V. Charbois, O. Klein, V. S. Tiberkevich, and A. N. Slavin, Phys. Rev. B **75**, 140405 (2007).
- [61] P. D. Drummond and D. F. Walls, J. Phys. A: Math. Gen. **13**, 725 (1980).
- [62] J.-P. Eckmann and D. Ruelle, Rev. Mod. Phys. **57**, 617 (1985).
- [63] P. Bryant, R. Brown, and H. D. I. Abarbanel, Phys. Rev. Lett. **65**, 1523 (1990).
- [64] H. J. Carmichael, *Statistical methods in quantum optics*, Springer (1999).
- [65] D. F. Walls and G. J. Milburn, *Quantum optics*, Springer (2008).
- [66] K. V. Kheruntsyan, J. Opt. B **1**, 225 (1999).
- [67] A. I. Lvovsky and M. G. Raymer, Rev. Mod. Phys. **81**, 299 (2009).
- [68] S. L. Braunstein and P. van Loock, Rev. Mod. Phys. **77**, 513 (2005).
- [69] A. Einstein, B. Podolsky, and N. Rosen, Phys. Rev. **47**, 777 (1935).
- [70] S. L. Braunstein, and H. J. Kimble, Phys. Rev. Lett. **80**, 869 (1998).
- [71] C. H. Bennett, H. J. Bernstein, S. Popescu, and B. Schumacher, Phys. Rev. A **53**, 2046 (1996).
- [72] G. Vidal, Phys. Rev. Lett. **83**, 1046 (1999).
- [73] G. Vidal, D. Jonathan, and M. A. Nielsen, Phys. Rev. A **62**, 012304 (2000).
- [74] A. Peres, Phys. Rev. Lett. **77**, 1413 (1996).
- [75] M. Horodecki, P. Horodecki, and R. Horodecki, Phys. Lett. A **223**, 1 (1996).
- [76] G. Vidal and R. F. Werner, Phys. Rev. A **65**, 032314 (2002).
- [77] J. Fiurasek, Phys. Rev. A **65**, 053818 (2002).
- [78] H. Lee, P. Kok, N. J. Cerf, and J. P. Dowling, Phys. Rev. A **65**, 030101 (2002).
- [79] T. E. Lee and H. R. Sadeghpour, Phys. Rev. Lett. **111**, 234101 (2013).
- [80] V. E. Demidov, H. Ulrichs, S. V. Gurevich, S. O. Demokritov, V. S. Tiberkevich, A. N. Slavin, A. Zhulud, and S. Urazhdin, Nat. Commun. **5**, 3179 (2014).
- [81] C. H. Bennett, D. P. DiVincenzo, J. A. Smolin, and W. K. Wootters, Phys. Rev. A **54**, 3824 (1996).
- [82] W. K. Wootters, Quantum Inf. Comput. **1**, 27 (2001).
- [83] K. Zyczkowski, Phys. Rev. A **60**, 27 (1999).
- [84] G. Adesso and F. Illuminati, Phys. Rev. A **72**, 032334 (2005).
- [85] J. Chen, C. Liu, T. Liu, Y. Xiao, K. Xia, G. E.W. Bauer, M. Wu, and H. Yu, Phys. Rev. Lett. **120**, 217202 (2018).
- [86] T. Yu, C. P. Liu, H. M. Yu, Ya. M. Blanter, and G. E. W. Bauer, Phys. Rev. B **99**, 134424 (2019).
- [87] J. L. Chen, T. Yu, C. P. Liu, T. Liu, M. Madami, K. Shen, J. Y. Zhang, S. Tu, M. S. Alam, K. Xia, M. Z. Wu, G. Gubbiotti, Ya. M. Blanter, G. E. W. Bauer, and H. M. Yu, arXiv:1903.00638.
- [88] E. Carlsson, S. Gevorgian, IEEE Trans. Microw. Theory Tech. **47**, 1544 (1999).
- [89] E. Langenberg, E. F.-Vila, V. Leboran, A. O. Fumega, V. Pardo, and F. Rivadulla, Appl. Phys. Lett. Mat. **4**, 104815 (2016).
- [90] A. Brataas, Y. Tserkovnyak, and G. E. W. Bauer, Phys. Rev. B **84**, 054416 (2011).
- [91] R. V. Smith, Cryogenics **9**, 11 (1969).
- [92] B. Baudouy, arXiv:1501.07153 (2015).
- [93] V. DAuria, S. Fornaro, A. Porzio, S. Solimeno, S. Olivares, and M. G. A. Paris, Phys. Rev. Lett. **102**, 020502 (2009).
- [94] J. Wenger, A. Ourjoumtsev, R. Tualle-Brouiri, and P. Grangier, Eur. Phys. J. D **32**, 391 (2005).
- [95] E. P. Menzel, F. Deppe, M. Mariantoni, M. A. A. Caballero, A. Baust, T. Niemczyk, E. Hoffmann, A. Marx, E. Solano, and R. Gross, Phys. Rev. Lett. **105**, 100401 (2010).
- [96] D. Bozyigit, C. Lang, L. Steffen, J. M. Fink, C. Eichler, M. Baur, R. Bianchetti, P. J. Leek, S. Filipp, M. P. da Silva, A. Blais, and A. Wallraff, Nat. Phys. **7**, 154 (2011).
- [97] E. P. Menzel, R. D. Candia, F. Deppe, P. Eder, L. Zhong, M. Ihmig, M. Haeberlein, A. Baust, E. Hoffmann, D. Ballester, K. Inomata, T. Yamamoto, Y. Nakamura, E. Solano, A. Marx, and R. Gross, Phys. Rev. Lett. **109**, 250502 (2012).
- [98] E. Hoffmann, F. Deppe, T. Niemczyk, T. Wirth, E. P. Menzel, G. Wild, H. Huebl, M. Mariantoni, T. Weiss, A. Lukashenko, A. P. Zhuravel, A. V. Ustinov, A. Marx, and R. Gross, Appl. Phys. Lett. **97**, 222508 (2010).
- [99] M. Mariantoni, E. P. Menzel, F. Deppe, M. A. A. Caballero, A. Baust, T. Niemczyk, E. Hoffmann, E.

- Solano, A. Marx, and R. Gross, *Phys. Rev. Lett.* **105**, 133601 (2010).
- [95] Y. Makhlin, G. Shon, and A. Shnirman, *Rev. Mod. Phys.* **73**, 357 (2001).
- [96] F. T. Arecchi, E. Courtens, R. Gilmore, and H. Thomas, *Phys. Rev. A* **6**, 2211 (1972).
- [97] S. Lloyd and S. L. Braunstein, *Phys. Rev. Lett.* **82**, 1784 (1999).
- [98] D. P. DiVincenzo, *Science* **270**, 255 (1995).
- [99] M. Kitagawa and M. Ueda, *Phys. Rev. A* **47**, 5138 (1993).
J. Esteve, C. Gross, A. Weller, S. Giovanazzi, and M. K. Oberthaler, *Nature* **445**, 1216 (2008).
M. F. Riedel, P. Bohi, Y. Li, T. W. Hansch, A. Sinatra, and P. Treutlein, *Nature* **464**, 1170 (2010).
- [100] L. Vaidman, *Phys. Rev. A* **49**, 1473 (1994).
A. Furusawa, J. L. Sørensen, S. L. Braunstein, C. A. Fuchs, H. J. Kimble, and E. S. Polzik, *Science* **282**, 706 (1998).
- [101] V. Giovannetti, S. Lloyd, and L. Maccone, *Science* **306**, 1330 (2004).
- [102] B. Vlastakis, G. Kirchmair, Z. Leghtas, S. E. Nigg, L. Frunzio, S. M. Girvin, M. Mirrahimi, M. H. Devoret, and R. J. Schoelkopf, *Science* **342**, 607 (2013).
- [103] R. McConnell, H. Zhang, J. Hu, S. Cuk, and Vladan Vuletic, *Nature* **519**, 439 (2015).
- [104] V. Veitch, C. Ferrie, David Gross, and Joseph Emerson, *New J. Phys.* **15** 039502 (2013).
- [105] X.-J. Liu, M. F. Borunda, X. Liu, and J. Sinova, *Phys. Rev. Lett.* **102**, 046402 (2009).
- [106] Z. Wu, L. Zhang, W. Sun, X.-T. Xu, B.-Z. Wang, S.-C. Ji, Y. Deng, S. Chen, X.-J. Liu, and J.-W. Pan, *Science* **354**, 83 (2016).
- [107] T. Yu, Y. M. Blanter, G. E. W. Bauer, arXiv:1909.00953 and arXiv:1909.01817.
- [108] C. Nayak, S. H. Simon, A. Stern, M. Freedman, and S. D. Sarma, *Rev. Mod. Phys.* **80**, 1083 (2008).
- [109] V. Peano, M. Houde, F. Marquardt, and A. A. Clerk, *Phys. Rev. X* **6**, 041026 (2016).
- [110] A. Kamra and W. Belzig, *Phys. Rev. Lett.* **116**, 146601 (2016).
- [111] G. Kirchmair, B. Vlastakis, Z. Leghtas, S. E. Nigg, H. Paik, E. Ginossar, M. Mirrahimi, L. Frunzio, S. M. Girvin, and R. J. Schoelkopf, *Nature* **495**, 205 (2013).
- [112] S. Streib, N. V.-Silva, K. Shen, and G. E. W. Bauer, , *Phys. Rev. B* **99**, 184442 (2019).
- [113] R. M. White and M. Sparks, *Phys. Rev.* **130**, 632 (1963).
- [114] C. B. d. Araujo, *Phys. Rev. B* **10**, 3961 (1974).
- [115] S. R. White, *Phys. Rev. Lett.* **69**, 2863 (1992).
S. R. White, *Phys. Rev. B* **48**, 10345 (1993).
U. Schollwock, *Ann. Phys.* **326**, 96 (2011).
- [116] M. Pozniak, K. Zyczkowski, and M. Kus, *J. Phys. A: Math. Gen.* **31**, 1059 (1998).